Analysis of the Impact of Seasat Scatterometer Data and Horizontal Resolution on GLA Model Simulations of the *QE II* Storm

ALLEN J. LENZEN AND DONALD R. JOHNSON*

Space Science and Engineering Center, University of Wisconsin—Madison, Madison, Wisconsin

ROBERT ATLAS

Laboratory for Atmospheres, Goddard Space Flight Center, Greenbelt, Maryland

(Manuscript received 9 January 1992, in final form 9 July 1992)

ABSTRACT

Quasi-Lagrangian diagnostics of mass, angular momentum, water vapor, and kinetic energy are evaluated for four different Goddard Laboratory for Atmospheres model simulations of the *Queen Elizabeth II* storm of 9–11 September 1978 to study the impact of *Seasat-A* satellite scatterometer (SASS) winds and horizontal resolution in numerical prediction. In a four-way comparison, the diagnostics investigate the impact of including dealiased SASS winds in the initial conditions of the model and doubling the horizontal resolution on 36 h simulations of the *QE II* storm. The largest impact on the simulation stemmed from doubling the model's horizontal resolution from 4° × 5° to 2° × 2.5°. The increased resolution resulted in a storm track much closer to that observed, a much deeper surface development, a stronger mass circulation, stronger heating, and stronger increase of angular momentum. The inclusion of SASS data resulted in an approximately 2–3-mb-deeper surface cyclone for both the 2° × 2.5° and 4° × 5° resolution simulations. The inclusion also led to substantial increases in the horizontal mass circulation and heating for the 2° × 2.5° simulation. During the early explosive deepening phase of the cyclone, the inward lateral transport of water vapor in lower layers was larger in the 2° × 2.5° SASS than in the 2° × 2.5° NOSASS (exclusion of SASS surface winds) simulation. During the period of most rapid development, the results from the SASS simulation revealed a larger generation of kinetic energy throughout the troposphere and increased outward transport of kinetic energy in upper layers.

1. Introduction

Intense and rapidly developing oceanic cyclones pose a serious threat to seafaring ships and coastal regions. Thus, accurate forecasting of these systems is important for shipping and safety. Although the reliability of numerical weather prediction (NWP) has improved substantially over the last several decades, NWP models still fail occasionally to accurately predict the rapidity and ultimate intensity of the development of such cyclones.

The intense ocean cyclone of 9–11 September 1978, which damaged the ocean liner *Queen Elizabeth II* and sank the trawler *Captain Cosmos,* is an example of a major ocean storm for which accurate prediction has proven to be difficult. This cyclone, known as the *QE II* storm, has been the subject of a number of diverse investigations in recent years. Previous studies have established the importance of accurate initial conditions, parameterization of subgrid-scale processes, and resolution (Anthes et al. 1983; Gyakum 1983, 1991; Helfand et al. 1987; Kuo et al. 1991; Uccellini 1986) for successful prediction of this storm. A number of investigations with both global and regional models have been conducted to evaluate the impact of Seasat data on the prediction of the *QE II* storm (Anderson et al. 1991; Duffy and Atlas 1986; Ingleby and Bromley 1991; Stoffelen and Cats 1991). The results of these studies have for the most part been mixed, with either negligible or positive impact reported. In general, the mechanism of Seasat data impact has not been evaluated in detail in any of the aforementioned studies.

The Seasat satellite was launched in June 1978 and provided data for a 96-day period, which included the period of the *QE II* storm. On board was the *Seasat-A* satellite scatterometer (SASS), which measured radar backscatter from centimeter-scale capillary waves. An empirical relationship was used to infer surface wind velocity from these measurements. This relationship, however, provided up to four possible directions (referred to as *aliases*) with each report. Thus, before this

* Also affiliated with Department of Atmospheric and Oceanic Sciences. University of Wisconsin—Madison, Madison, Wisconsin.

Corresponding author address: Allen J. Lenzen, Space Science and Engineering Center, University of Wisconsin—Madison, 1225 West Dayton Street, Madison, WI 53706.

data could be used in meteorological analyses, this ambiguity in direction had to be removed. At the Goddard Laboratory for Atmospheres (GLA) an objective procedure to remove the directional ambiguity of SASS data, which made use of a first guess provided by the GLA general circulation model, was developed. The GLA analysis–forecast system was then used to assimilate the 96 days of SASS observations and to generate global gridded fields of ocean surface wind and fluxes based on this data (Atlas et al. 1987).

Early SASS data impact studies with global models showed a generally negligible impact of these data in the Northern Hemisphere (Baker et al. 1984; Duffy et al. 1984; Yu and McPherson 1984). But the later regional model study of Duffy and Atlas (1986) demonstrated for the first time a positive impact of SASS surface winds on the prediction of the *QE II* storm. This impact was shown to result from the vertical extension of the influence of the SASS surface wind data to higher levels using a simple statistical procedure. It was not clear, however, whether the use of such a procedure would lead to a beneficial impact of SASS data in a global model. Recently, the impact of SASS data has been revisited with an improved version of the GLA analysis–forecast system that incorporated limited extension of SASS data in the vertical. These experiments show a small positive impact of SASS data on GLA model forecasts, including a modest improvement of the *QE II* storm prediction.

This paper presents a detailed evaluation of the impact of both SASS surface wind data and increased horizontal resolution on GLA model predictions of the *QE II* storm in order to ascertain the underlying reasons for this positive SASS impact. For this purpose, the impact evaluation is based on quasi-Lagrangian diagnostics of mass, angular momentum, water vapor, and kinetic energy that were developed by Johnson and Downey (1975a,b). The quasi-Lagrangian approach distinguishes development from the effects of translation that complicate the interpretation of results from an Eulerian analysis. These diagnostics have previously been used in studies of extratropical cyclone development (Johnson et al. 1976; Johnson and Hill 1987; Hale 1983) and the evaluation of the impact of satellite temperature soundings on model cyclone prediction (Vergin et al. 1984).

In section 2, the description of the model and the inclusion of dealiased Seasat winds are presented. The preparation of the isentropic dataset is presented in section 3. The results of the quasi-Lagrangian analysis are presented in section 4. A brief synoptic description of the four simulations is given in section 4a. In section 4c, the isentropic lateral mass transport and heating are presented. The angular momentum, water vapor, and kinetic energy budgets are presented in sections 4d, 4e, and 4f, respectively. A discussion of the results of the quasi-Lagrangian diagnostics are presented in section 5.

2. Description of the experiment

The objective of this investigation is to ascertain the underlying reasons for the positive impact of the SASS wind data and increased horizontal resolution on large-scale numerical model predictions of the *QE II* cyclone through quasi-Lagrangian diagnostics of mass, angular momentum, water vapor, and kinetic energy. For this study a version of the GLA analysis–forecast system is used to assimilate all available conventional and satellite data and to generate forecasts of the *QE II* storm. This system consists of an objective analysis scheme that uses continuity provided by a model's first-guess forecast. Earlier versions of this system used a two-dimensional, univariate, successive corrections method of analysis (Baker et al. 1984). The version used in this study differs primarily in that a three-dimensional, multivariate optimum interpolation (OI) analysis scheme is used to assimilate all conventional and satellite data. This scheme is described in detail by Baker et al. (1987) and has previously been used in the assimilation of First GARP (Global Atmospheric Research Program) Global Experiment (FGGE) data.

The model used for both assimilation and prediction is the GLA fourth-order general circulation model. This model is described in detail by Kalnay et al. (1983) and has been used in previous studies of satellite data impact (e.g., Halem et al. 1982; Atlas et al. 1985, 1987; Baker et al. 1984, 1987) and of cyclogenesis (Atlas 1987).

The hydrodynamics of the model is based on the energy-conserving scheme of Kalnay-Rivas et al. (1977), which computes horizontal differences to fourth-order accuracy. In this scheme, wavelengths longer than four grid lengths are resolved accurately without damping. Wavelengths shorter than four grid lengths, which would otherwise be grossly misrepresented by the finite differences, are removed by filtering while they are still infinitesimal. This treatment of the shortest waves avoids the accumulation of energy that would otherwise occur at the short-wave cutoff. The vertical coordinate is a terrain-following σ-pressure coordinate with nine equally spaced levels. Even though there is no explicit balancing of the wind and mass field in the assimilation cycle, the use of the Euler backward time scheme during the model integration damps most of the gravity waves, and the vertical-motion field is well correlated with the synoptic patterns. This procedure, which is analogous to dynamic initialization, avoids the elimination of large-scale divergence fields driven by heating, which occurs in current applications of nonlinear normal-mode initialization. The model contains a complete range of subgrid-scale physical parameterizations, as presented in detail by Kalnay et al. (1983) and summarized in Helfand et al. (1987).

Two different horizontal resolution versions of the GLA fourth-order model are used in the current study.

A 4° latitude × 5° longitude version was used for data assimilation, while both 4° × 5° and 2° × 2.5° versions were used to generate forecasts of the *QE II* storm.

Two assimilation cycles, referred to as SASS and NOSASS were performed from 0000 UTC 7 September to 0000 UTC 9 September 1978. For the SASS experiment, all available conventional data, satellite temperature sounding data, and unambiguous SASS surface wind vectors were assimilated. The unambiguous SASS data were obtained from the previous 96-day assimilation that had been performed by Atlas et al. (1987) to remove the directional ambiguity associated with each SASS report. The NOSASS assimilation was identical to the SASS experiment except for the exclusion of the SASS surface winds. Thirty-six-hour forecasts using both the 4° × 5° and 2° × 2.5° versions of the GLA fourth-order model were then generated from both the SASS and the NOSASS analyses at 0000 UTC 9 September 1978 in an attempt to simulate the large-scale aspects of the *QE II* cyclone development and displacement.

3. Isentropic dataset

For the isentropic quasi-Lagrangian analysis, data were interpolated from sigma to isentropic coordinates at 5-K increments from 265 to 385 K by assuming that T, u, and v varied linearly with pressure raised to the R/c_p power. Since the tropopause in the model for the region of the *QE II* cyclone development was in the range of 350 K and mass values in isentropic layers above this level were small, diagnostics will be presented only up to 360 K. The resolution in the GLA model being limited with nine levels does not warrant diagnostics in the stratosphere above the 360-K surface.

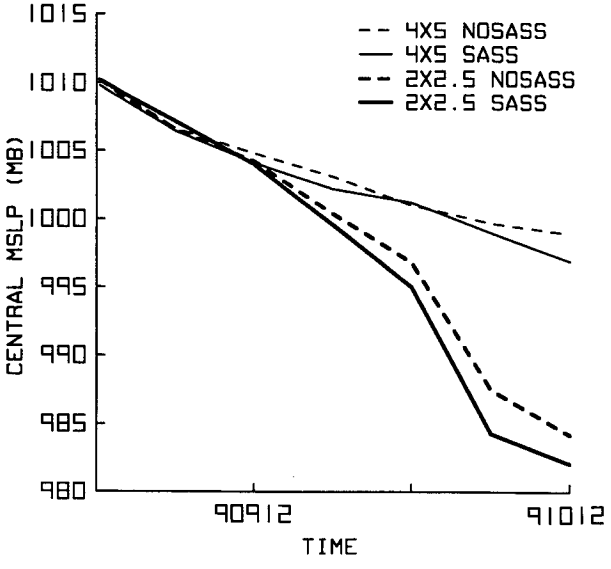

FIG. 1. Time series of minimum sea level pressure (mb) for GLA simulations of the *QE II* storm.

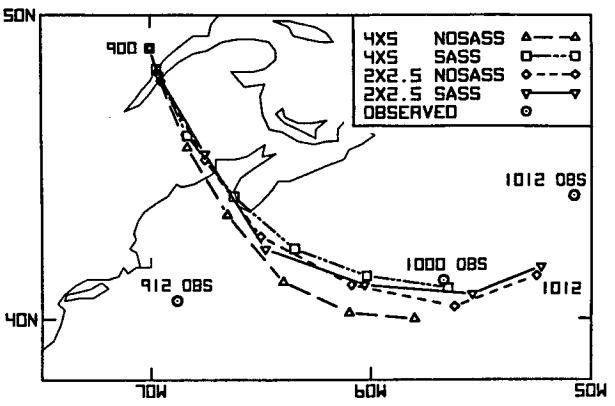

FIG. 2. Storm tracks of the *QE II* storm for 2° × 2.5° SASS (del), 2° × 2.5° NOSASS (diamond), 4° × 5° SASS (box), and 4° × 5° NOSASS (triangle) simulations. Observed track (circle) from Gyakum (1983).

Since surface winds are not determined prognostically in the model, surface winds were extrapolated from winds at the lowest two sigma levels. In the case of superadiabatic conditions in the surface layer, the surface potential temperature was adjusted by setting the surface potential temperature to be 0.001 K less than the potential temperature at the first sigma level.

4. Results

a. Model simulations

The central pressure of the four predicted cyclones, the storm tracks, and the 36-h predicted sea level pressure are shown in Figs. 1, 2, and 3, respectively. The surface cyclone for the four simulations deepened at approximately the same rate during the first 12 h. The surface cyclone for the 2° × 2.5° simulations deepened explosively from 1200 UTC 9 September through 0600 UTC 10 September, with the largest deepening occurring between 0000 UTC 10 September and 0600 UTC 10 September. The deepening rate for the 4° × 5° SASS simulation increased somewhat after 0000 UTC 10 September; however, the deepening rate for either 4° × 5° simulation was much less than for the 2° × 2.5° simulations. The 2° × 2.5° SASS simulation developed the deepest surface cyclone at 36 h with a central pressure of 982 mb, which was 37 mb higher than the observed mean central pressure of 945 mb (Gyakum 1983).[1] The storm tracks of the 2° × 2.5° simulations were similar, with the cyclone moving to the southeast and then moving more easterly as the cyclone rapidly developed. The movement of the surface cyclone in

[1] Other global models initialized at 0000 UTC 9 September 1978 simulated similar intensities for the *QE II* storm. The ECMWF T106 model simulated a central pressure of 988 mb, while the NMC T80 model simulated a central pressure of 988 mb without SASS data, and 985 mb with SASS data included in the initial conditions (T. Yu 1991, personal communication).

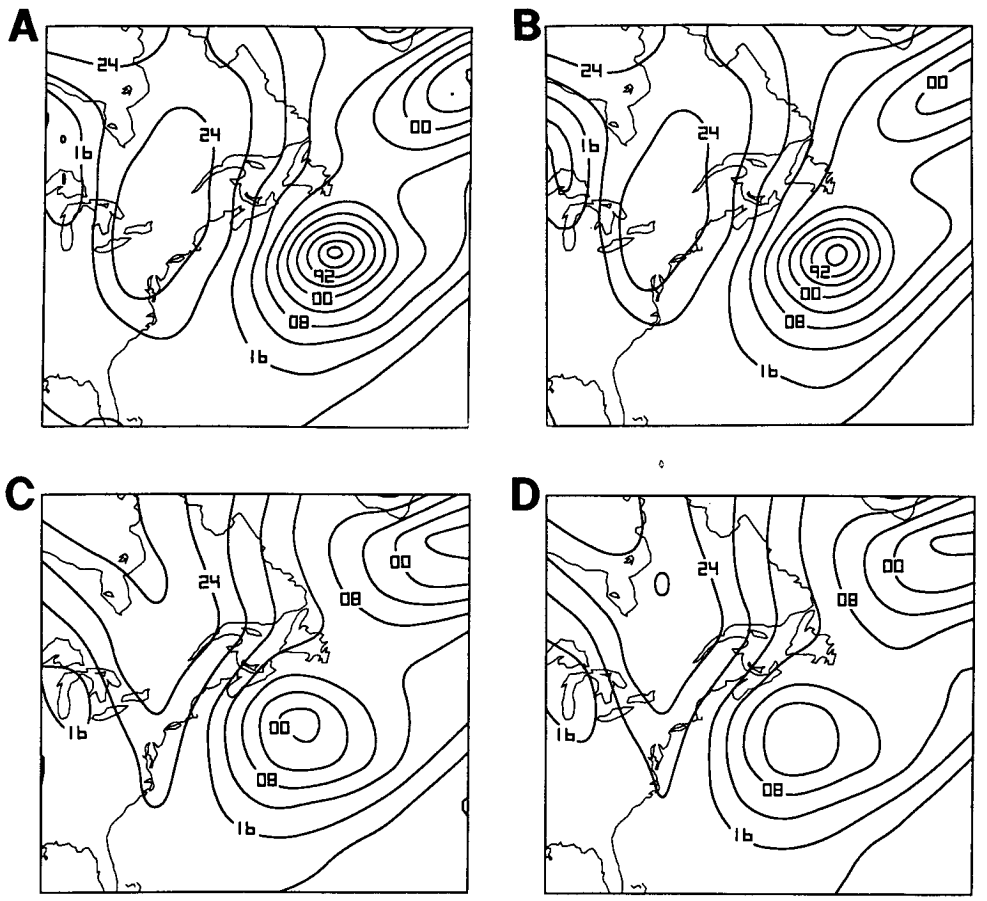

FIG. 3. Thirty-six-hour predicted mean sea level pressure (mb) of the *QE II* storm at 1200 UTC 10 September 1978 for (a) 2° × 2.5° SASS, (b) 2° × 2.5° NOSASS, (c) 4° × 5° SASS, and (d) 4° × 5° NOSASS simulations.

the 4° × 5° simulations was much slower than in the 2° × 2.5° simulations. The 4° × 5° NOSASS model storm track was south of that observed and resulted in the largest position error of the 36-h forecasts. Of the four simulations, the 2° × 2.5° SASS simulation provided the best prediction of the *QE II* cyclone. In this case, the cyclone deepened to the lowest mean sea level pressure and the storm track was the closest to the observed.

Gyakum (1991) has described the mesoscale structure of the antecedent development of the *QE II* storm for the period 0000 UTC to 1200 UTC 9 September 1978. This analysis depicted two developing surface cyclones. The southern cyclone subsequently explosively deepened after 1200 UTC 9 September to form the *QE II* storm. The northern cyclone deepened during this period and moved southeastward from Quebec toward Nova Scotia, eventually losing its identity to the southern cyclone. To determine if a similar evolution was evident in the initial 12 h of the GLA simulations, the mean sea level pressure pattern and winds at the lowest model sigma level were examined (not shown). With the coarse horizontal and vertical resolution of the 2° × 2.5° and 4° × 5° GLA model simulations, it was not possible to identify a closed surface circulation that corresponded to Gyakum's southern cyclone for the first 12 h. Therefore, the cyclone that was resolvable at the scales of the GLA model (this corresponds closely with what Gyakum called the northern surface cyclone for the period 0000 to 1200 UTC 9 September) was chosen to determine the storm track for the quasi-Lagrangian diagnostics for this early period. Since the model is spinning up and adjusting to initial conditions during part of the first 6–12 h of the forecast, less emphasis is given in the discussion of the diagnostics for this period.

Since the largest weights for the Seasat winds were assigned to the lowest sigma layers and the maximum differences in the water vapor transport (to be discussed in section 4e) between the SASS and NOSASS simulations occurred at the lowest layers, streamlines and isotachs for the lowest sigma layer are shown in Figs. 4a and 4b for 0000 UTC 9 September 1978. The 2° × 2.5° SASS initial wind field has a much stronger

ridge over the western Atlantic Ocean than in the NOSASS initial wind field resulting in more southerly winds just off the east coast of the United States. In this region, the resultant difference in the wind vector at this level is 3 m s^{-1} from the southeast (Fig. 4c). Maximum differences of 7 m s^{-1} occur over the central Atlantic Ocean. These are associated with the stronger trough of low pressure in the central Atlantic in the SASS simulation compared to the NOSASS.

b. *Quasi-Lagrangian diagnostics*

The definitions and budget equations for the quasi-Lagrangian budget diagnostics (Johnson and Downey 1975a,b) of mass, angular momentum, water vapor, and kinetic energy are presented in appendix A. A list of symbols is presented in appendix B. The budget diagnostics compared in the next sections emphasize the differences in the quasi-Lagrangian transport of the various properties that stem from inclusion of the SASS data and doubling the horizontal resolution. As Johnson and Downey (1975a) emphasized and later results have verified (e.g., Johnson and Hill 1987), the exchange of mass and angular momentum in storms is closely linked with the larger-scale geostrophic nature of isentropic mass circulations of the larger-scale planetary circulation. Most of the vertical time sections presented will be for quantities integrated over 5-K isentropic layers.

Previous quasi-Lagrangian diagnostic studies of extratropical cyclones have isolated two types of development (Johnson et al. 1976). The first type called leeside *dry baroclinic* development is characterized by inward lateral mass transport in higher isentropic layers, outward lateral mass transport in lower isentropic layers, and downward or weakly upward diabatic mass transport. The second type called *moist baroclinic* development is characterized by inward lateral mass transport in lower isentropic layers, outward lateral mass transport in upper isentropic layers, and upward diabatic mass transport from lower isentropic layers to upper isentropic layers. Both types of development were observed in a cyclone developing over Alberta in the lee of the Rockies (Johnson et al. 1976) and in a model cyclone prediction analyzed by Vergin et al. (1984). In both cases, the dry baroclinic development stage preceded the moist baroclinic development stage. In many cases of continental cyclone development, only a stage of moist baroclinic development is observed (e.g., Johnson and Downey 1976; Hale 1983; Johnson and Hill 1987).

c. *Isentropic mass budget*

The isentropic time section of the area-averaged pressure (Fig. 5a) for the 2° × 2.5° SASS simulation provides a relative measure of the vertical distribution of the various isentropic surfaces. Pressure on an is-

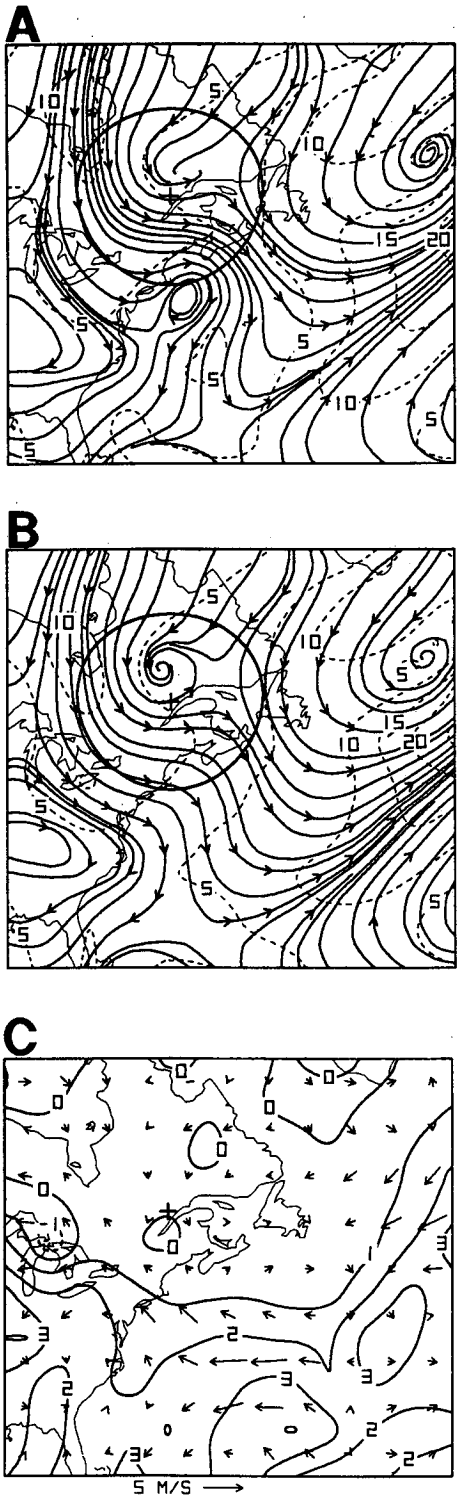

FIG. 4. Streamlines (solid) and isotachs (dashed, contour interval 5 m s^{-1}) for the lowest model sigma layer at 0000 UTC 9 September 1978 for (a) 2° × 2.5° SASS, (b) 2° × 2.5° NOSASS simulations, and (c) difference fields of wind (arrows) and water vapor (g kg^{-1}) for lowest sigma layer for 2° × 2.5° SASS minus 2° × 2.5° NOSASS. Areal location of 7.5° budget volume is indicated by circle.

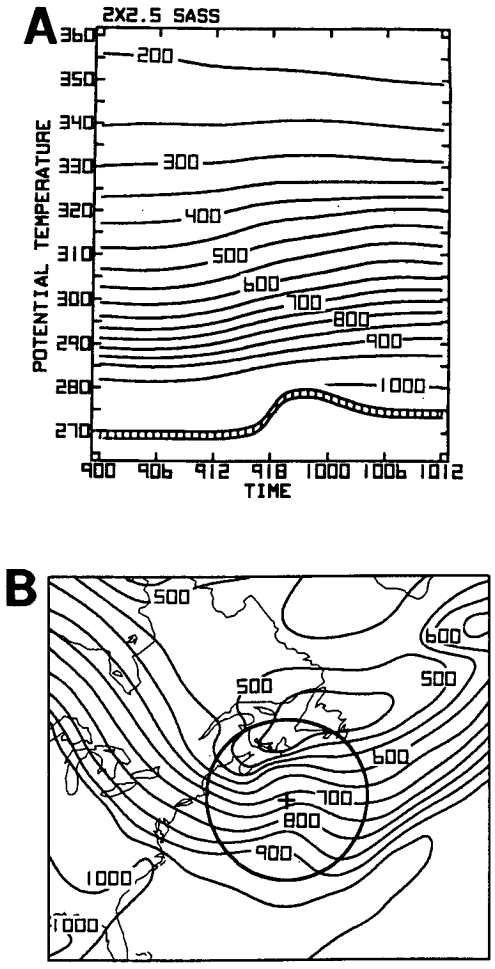

FIG. 5. (a) Isentropic time section of area-averaged pressure (mb) for a 7.5° budget volume for 2° × 2.5° SASS simulation. Double line with vertical hatching near bottom of figure indicates coldest surface potential temperature within the budget volume. (b) Pressure on the 300-K isentropic surface at 0000 UTC 10 September 1978 for 2° × 2.5° SASS simulation. Areal location of 7.5° budget volume is indicated by circle.

entropic surface, however, varies horizontally, as demonstrated in Fig. 5b. For example, the pressure on the 300-K isentropic surface for 0000 UTC 10 September varies from 440 mb in the northern part of the volume to 930 mb in the southern part of the volume, with an areal mean of approximately 700 mb.

The time section of the isentropic lateral mass transport (adjusted for mass balance) for the 2° × 2.5° SASS simulation (Fig. 6a) shows a layer of inward mass transport that extends from roughly 290 to 300 K, which increases in magnitude and vertical extent as the cyclone develops. Immediately above this layer, the lateral mass transport is outward and also increases in magnitude with time. Beginning with the period of maximum development at 0000 UTC 10 September, the mass circulation of the 2° × 2.5° SASS simulation has become well organized throughout the troposphere, with inflow below 305 K and outflow above. The outward mass transport below 290 K, which is evident in all four time sections during the initial 24 h, is a reflection of the movement of the surface cyclone from the North American continental region toward the Atlantic Ocean and the relative movement of the coldest air from the storm region by this process.

In the four-way comparison (Fig. 6), the primary differences in the storm relative mass transport stem from the effect of doubling the horizontal resolution. Note that the intensity of the inward and outward lateral mass transports in the troposphere is generally larger and better organized in the 2° × 2.5° than in the 4° × 5° simulations. Overall, the SASS and NOSASS mass circulations at 2° × 2.5° are in relatively close agreement with each other, as are the two mass circulations at 4° × 5°. Within the paired simulations, differences in the intensity and organization of the inward and outward branches of the mass circulation for the 2° × 2.5° resolution are evident beyond 1800 UTC 9 September. The maximum intensity of the inward transport between 290 and 300 K is 12×10^9 kg s^{-1} at 0000 UTC 10 September for SASS, while it is only 8×10^9 kg s^{-1} for NOSASS. Likewise, the outflow region with values greater than 4×10^9 kg s^{-1} is more vertically and temporally extended in the SASS than in the NOSASS time section. Thus, the inward and outward lateral mass transports in the troposphere are more intense for the 2° × 2.5° SASS than for the 2° × 2.5° NOSASS simulation. The potential temperatures of the inward branch are characteristic of the oceanic boundary-layer surface potential temperatures; therefore, this increased inward transport is likely due to insertion of SASS winds, which intensified the horizontal mass convergence within the cyclone's planetary boundary layer over the ocean. These forecast differences at 36 h likely reflect the impact of the SASS winds on the mass circulation within a model possessing adequate resolution to dynamically develop a more intense vortex circulation over the 36-h period. The limited resolution of the 4° × 5° GLA model was not capable of capturing this aspect of the positive impact of the SASS data.

The mass-weighted area-averaged heating rate $\dot{\theta}$ for all four simulations (Fig. 7) is computed from vertical integration of the quasi-Lagrangian isentropic mass continuity equation over the budget volume (Johnson and Downey 1975a). After 0600 UTC 9 September, the heating rate becomes positive in the 280–325-K layer and increases with time until 0300 UTC 10 September for the 2° × 2.5° simulations and until 2100 UTC 9 September for the 4° × 5° simulations. For the 2° × 2.5° SASS and NOSASS forecasts, the heating rates reach a maximum of 18 and 13 K day^{-1}, respectively. The rate of 18 K day^{-1} is comparable to the maximum heating rate found by Hale (1983) for

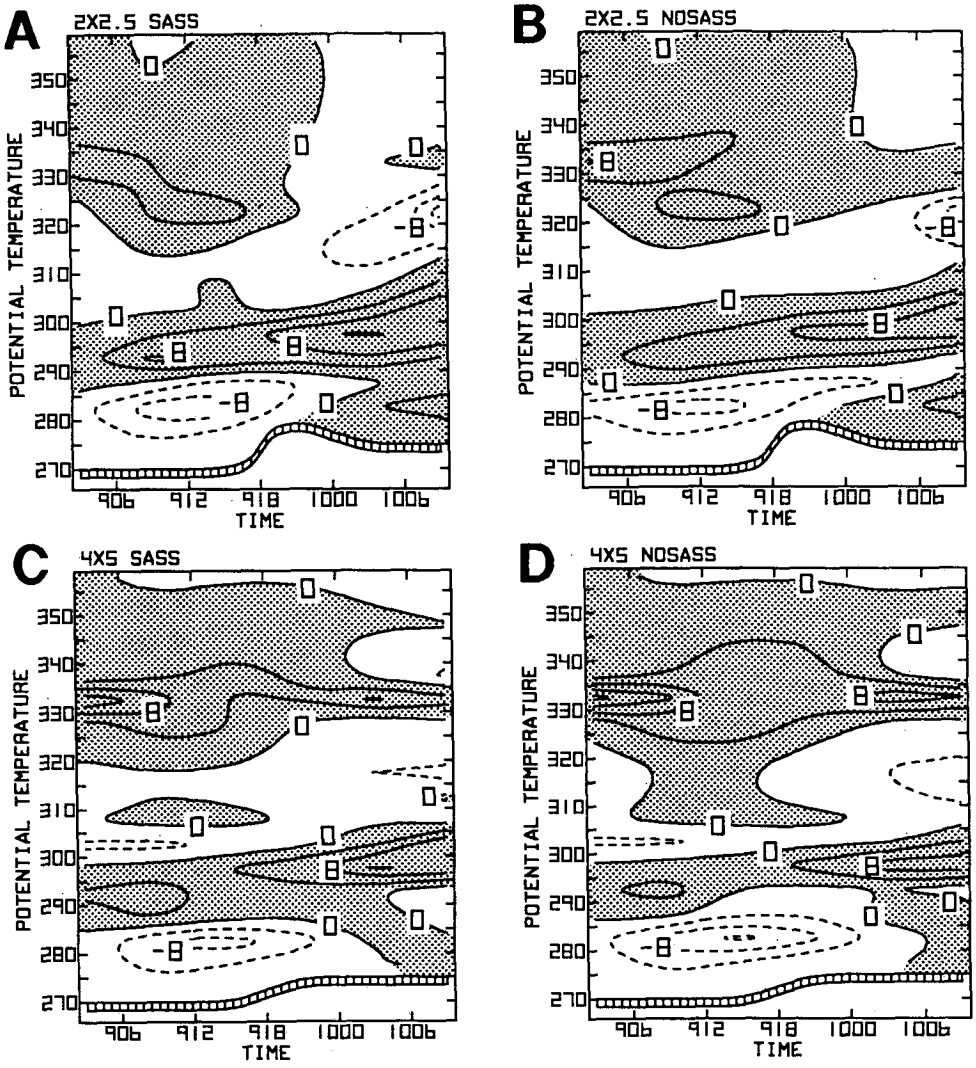

FIG. 6. Isentropic time sections of lateral mass transport (10^9 kg s^{-1}) for a 7.5° budget volume for (a) 2° × 2.5° SASS, (b) 2° × 2.5° NOSASS, (c) 4° × 5° SASS, and (d) 4° × 5° NOSASS simulations. Regions of inward transport are stippled. Double line with vertical hatching near bottom of figure indicates coldest surface potential temperature within budget volume.

the intense Ohio Valley snowstorm of 25–27 January 1978. In the 4° × 5° simulations, where patterns were less organized, the effect on heating from adding the SASS data was substantially less. In the SASS simulations, the doubling of the horizontal grid resolution produced almost a doubling in the heating produced.

In the comparison of the timing of heating, the increase of heating in the 2° × 2.5° SASS simulation, as evidenced by the 8 K day^{-1} isopleth, precedes the increase in the other simulations by 6 h. The evidence of the earlier timing and larger amount of heating in the 2° × 2.5° SASS simulation over the other simulations indicates that the combination of SASS data and higher resolution has directly increased the intensity of the diabatically forced component of the isentropic mass circulation.

d. Angular momentum budget

An extension of work by Eliassen (1951) provides a relationship between torques and the forcing of the lateral mass transport in a hydrodynamically stable vortex (Johnson 1974; Gallimore and Johnson 1981). With respect to the distribution of torques along a surface of constant angular momentum, motion will be forced away from the axis of rotation where the torque is a maximum and toward the axis of rotation where the torque is a minimum (Fig. 8). Heating forces mass

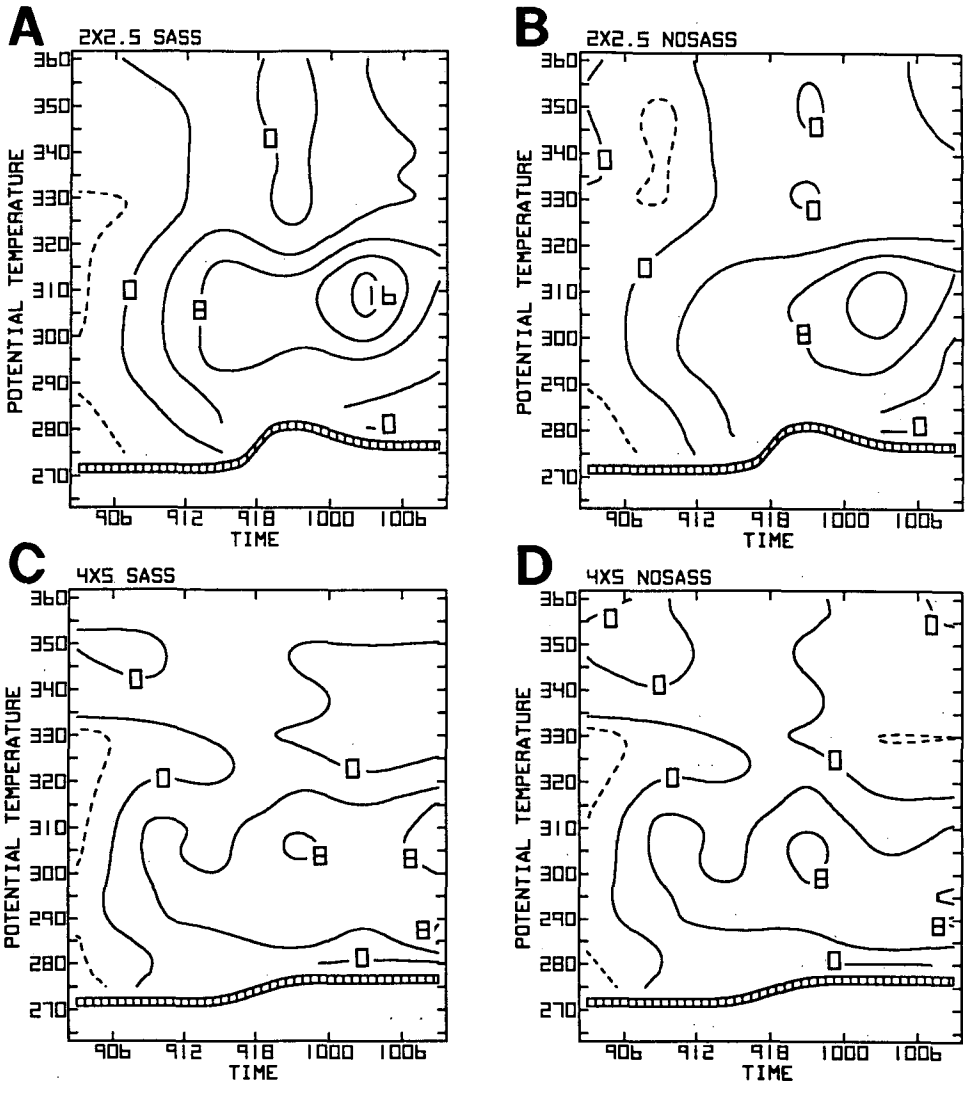

FIG. 7. Isentropic time sections of mass-weighted area-averaged heating (K day^{-1}) as in Fig. 6.

transport upward through the isentropic stratification along surfaces of constant angular momentum.

The vertical time section of the total torque (Fig. 9) (the sum of the pressure, inertial, and frictional torques and the convergence of the eddy mode of lateral angular momentum transport) shows a good correspondence between regions of maximum values of the total torque and regions of outward lateral mass transport and between regions of minimum total torque and regions of inward lateral mass transport. The magnitude of the torque tends to correspond with sign reversed to the magnitude of the lateral mass transport. The intensities of the positive and negative total torques are somewhat larger for the 2° × 2.5° SASS simulation than for the 2° × 2.5° NOSASS simulation. The total torque distributions for the 2° × 2.5° simulations depict a simpler temporal and vertical structure than those for the 4° × 5° simulations.

The diagnostics indicate that the best results were obtained for the SASS simulation at 2° × 2.5° resolution. Overall, the 2° × 2.5° mass circulations, the patterns of heating, and the torque distributions were more intense and better organized than the corresponding patterns for the 4° × 5° resolution. The higher horizontal resolution and inclusion of SASS winds together yielded a mass circulation that was substantially stronger with larger heating rates. This result supports the improved storm prediction with the inclusion of SASS data.

In order to identify processes that contributed to the total torque distributions, vertical time sections of the pressure and inertial torques and eddy mode of lateral

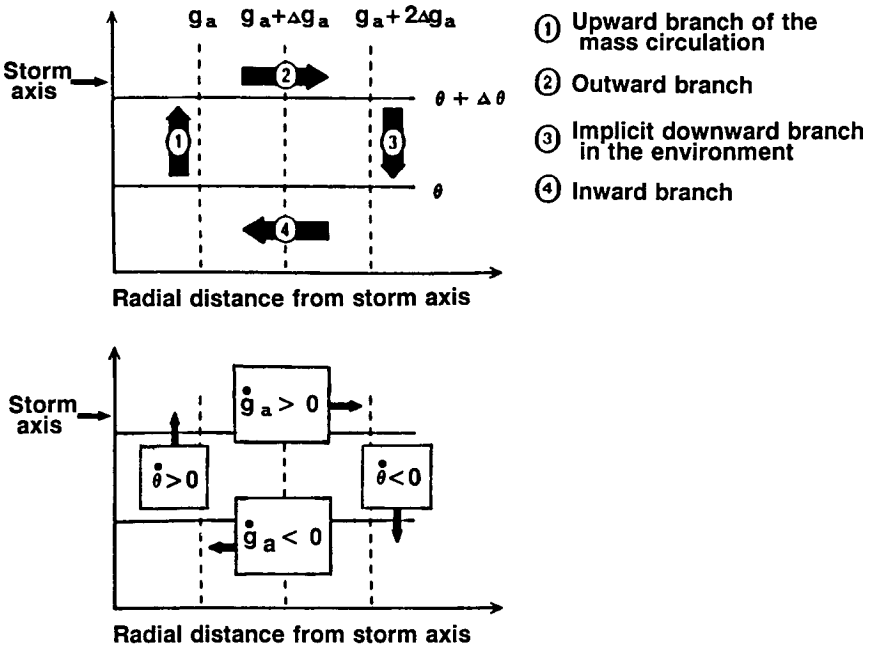

FIG. 8. Schematic illustrating Eliassen's perspective of the forcing of a vortex. Here g_a is absolute angular momentum and θ is potential temperature (after Johnson and Hill 1987).

absolute angular momentum transport are presented. Differences that resulted due to changes in horizontal resolution and inclusion of SASS data will be evident.

The areally integrated pressure torque results from the covariance between the azimuthal pressure gradient force and the mass within an isentropic layer. Since the volume-integrated pressure torque over flat terrain vanishes, a positive pressure torque in one layer implies a negative pressure torque in other layers (Johnson and Downey 1976). The general idealized vertical distribution of the pressure torque in the moist baroclinic development stage of continental extratropical cyclones is three layered, with negative torques in the lowest isentropic layers and in the upper isentropic layers, and a positive torque in the middle isentropic layers (Katzfey 1978; Wash 1978).

The isentropic time sections of the pressure torque (Fig. 10) for all four simulations have primarily a three-layered structure. The positive pressure torque in middle isentropic layers stems from the transfer of angular momentum by pressure stresses from upper isentropic layers to lower isentropic layers. A layer of negative pressure torque with relatively smaller magnitude and vertical extent exists below 285 K. The temporal and vertical structure of the pressure torque is more coherent for the 2° × 2.5° than for the 4° × 5° simulations. Major differences in the pressure torque distributions are evident between the 2° × 2.5° and 4° × 5° simulations. The positive torque in middle isentropic layers develops through a deeper isentropic layer but with a smaller maximum magnitude for the 2° × 2.5° compared to the 4° × 5° simulations. The time of maximum magnitude of the positive and negative torques tends to occur slightly earlier in the 2° × 2.5° than in the 4° × 5° simulations.

The inertial torque is an apparent torque that arises from the movement or acceleration of the cyclone through an asymmetric mass distribution. The magnitude and vertical structure of the inertial torque are determined by the covariance of the mass field with the motion and acceleration of the cyclone. For a hydrostatic atmosphere with a symmetric surface pressure distribution, the volume-integrated inertial torque is zero (Johnson and Downey 1975b).

The time sections of the inertial torque (Fig. 11) have a two-layered structure before 1800 UTC 9 September, and a three-layered structure thereafter. The inertial torque, with large positive values below 290 K and negative values above, is consistent with the forcing of the outward and inward mass transport above and below 290 K that occurs through the relative movement of the storm from cold continental air masses toward warmer oceanic air masses. In the lower layer, the positive inertial torque for the 4° × 5° NOSASS simulation is larger due to the errant more southerly track that increases the relative storm motion away from the low-level cold air that lies to the north of the storm. After 1800 UTC 9 September, a layer of positive inertial torque appears above 330 K. Below 325 K for the 2° × 2.5° simulations, the regions with larger values of the negative torque are deeper and better organized.

The eddy mode of lateral absolute angular momen-

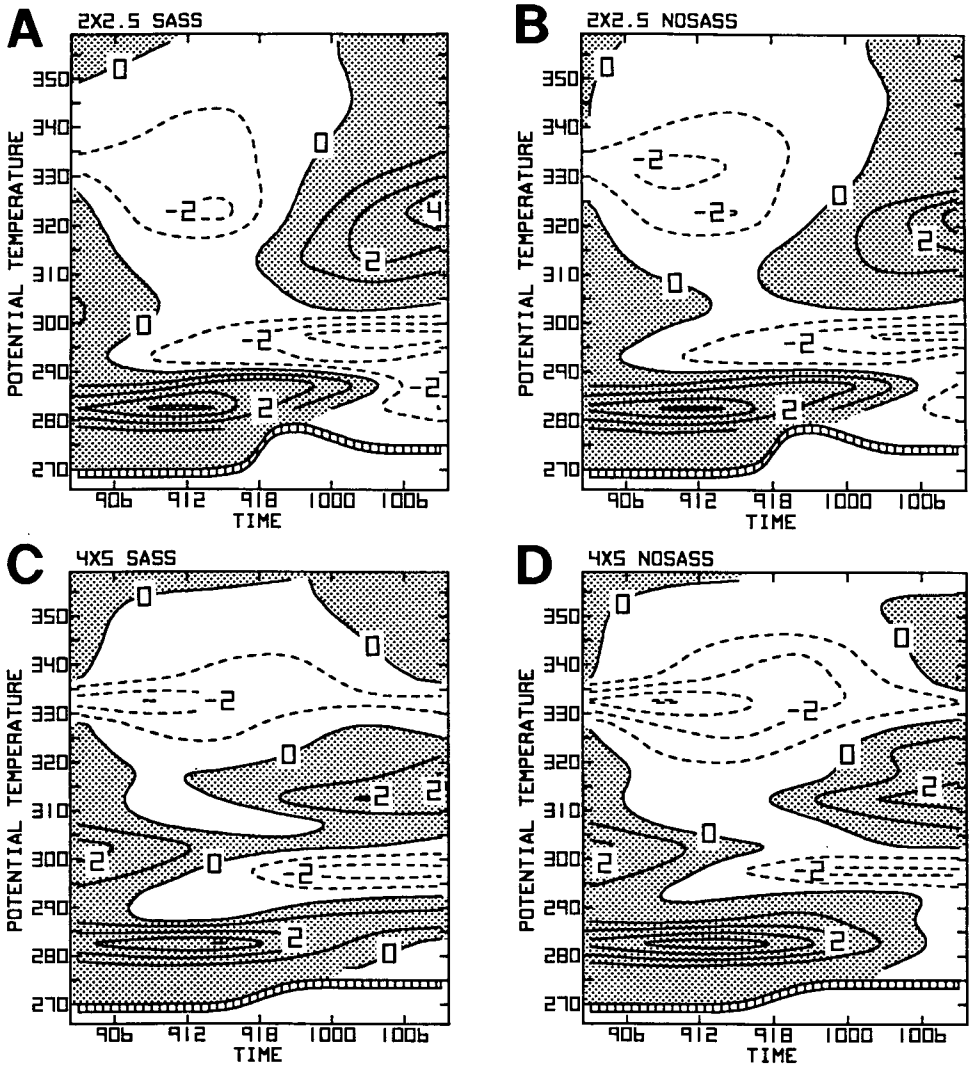

FIG. 9. Isentropic time sections of total torque (10^{17} kg m^2 s^{-2}) as in Fig. 6. Regions of positive torque are stippled.

tum transport is defined as the azimuthally integrated covariance between the azimuthal deviations of the radial and tangential components of the wind. The time sections of the eddy mode of lateral absolute angular momentum transport (Fig. 12) show a two-layered structure with negative values in lower isentropic layers and positive values in upper layers. The absolute magnitudes for both the positive and negative torques are greater for the 2° × 2.5° than for the 4° × 5° simulations. The eddy mode is somewhat stronger for 2° × 2.5° SASS than for 2° × 2.5° NOSASS. The inward eddy mode of lateral transport of angular momentum in upper layers has been linked with the rotation and deformation of the thermal structure by the low-level circulation of the developing cyclone (Johnson and Hill 1987; Wash 1978). The rotation and deformation of the thermal field lead to an S-shaped thermal-wind field, a characteristic feature of the self-development process (Palmén and Newton 1969). This leads to a covariance between the azimuthal deviation of the radial and tangential components of the geostrophic wind in upper levels (illustrated schematically in Fig. 13). The increase of the upper-level eddy mode is associated in part with the increased rotation of the low-level baroclinic zone by the more intense low-level mass circulation of the 2° × 2.5° simulations. The 2° × 2.5° simulations with higher spatial resolution better capture the intensity and rotation of the low-level baroclinic zone as the cyclone develops and impacts the intensity of the eddy mode. Also, the spinup of the low-level circulation in the 2° × 2.5° SASS simulation is stronger due to the more intense inward lateral mass and mean

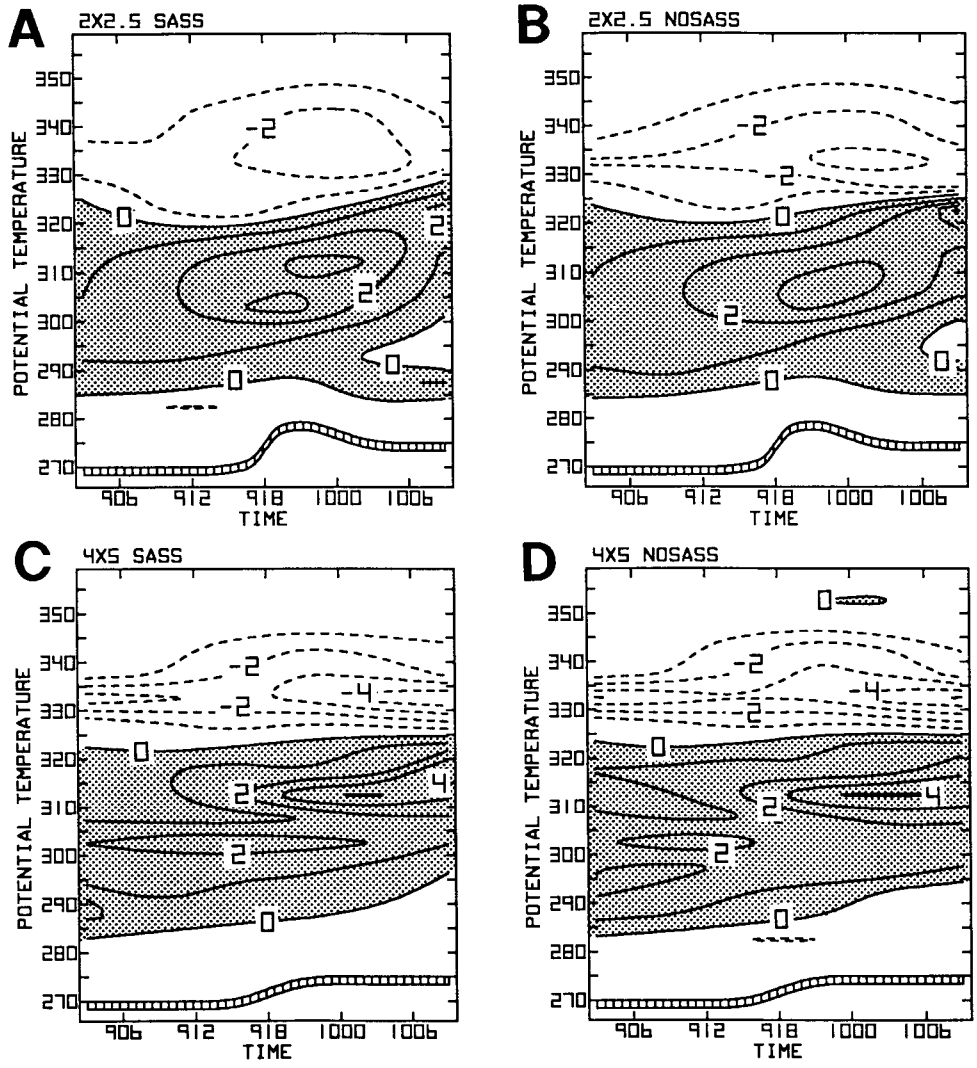

FIG. 10. Isentropic time sections of pressure torque (10^{17} kg m^2 s^{-2}) as in Fig. 9.

mode of absolute angular momentum transport that increases the rotation of the low-level baroclinic zone.

During the 36-h simulation, the relative importance of the constituent parts of the total torque varies. Before 0000 UTC 10 September, the positive inertial torque below 290 K is larger in magnitude than the sum of the negative frictional torque (not shown), eddy mode of lateral transport, and the pressure torque leading to a positive total torque. After 0000 UTC 10 September, the sum of the negative frictional torque, eddy mode, and pressure torque below 290 K is larger in magnitude than the inertial torque leading to a negative total torque. In the 290–300-K layer, the large negative eddy mode, negative inertial, and frictional torques are larger in magnitude than the positive pressure torque leading to a negative total torque. In the 300–310-K layer between 900 to 1800 UTC 9 September, the negative eddy mode and inertial torque are slightly larger in magnitude than the positive pressure torque leading to a negative total torque. Before 1800 UTC 9 September, in the 310–320-K layer the negative inertial torque is larger in magnitude than the sum of the positive pressure torque and weak positive eddy mode leading to a negative total torque. Above 320 K, the sum of the negative inertial and pressure torque is larger in magnitude than the positive eddy mode, leading to a negative total torque. In the 305–320-K layer after 1800 UTC 9 September, the positive pressure torque and positive eddy mode dominate to give a positive total torque. Above 320 K after 1800 UTC 9 September, the positive eddy mode dominates.

The vertical profiles of mass-weighted area-averaged relative angular momentum (Fig. 14a) for 0000 UTC 9 September show similar profiles for both the 2°

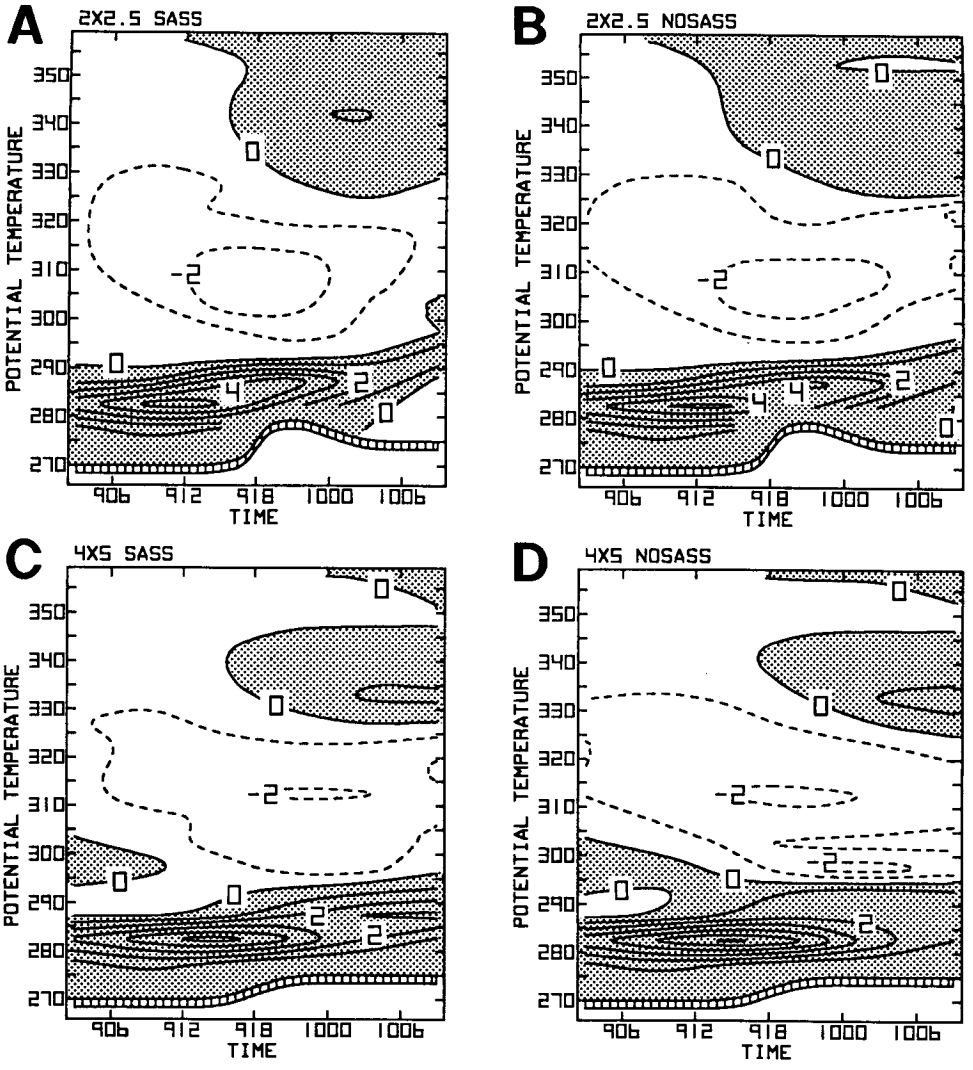

FIG. 11. Isentropic time sections of inertial torque (10^{17} kg m^2 s^{-2}) as in Fig. 9.

$\times$ 2.5° and 4° $\times$ 5° SASS simulations for the 7.5° budget volume. The small values in the lower isentropic layers reflect the lack of a significant low-level circulation in the initial state. The larger values in the upper isentropic layers are associated with the upper-level jet streaks and their configuration with respect to the development of the cyclone in a region of positive relative vorticity. The contrast of the vertical profiles of the relative angular momentum on 1200 UTC 10 September (Fig. 14b) with the initial state profiles shows the strong spinup of the low-level vortex during the 36-h forecast. Low-level increases of relative angular momentum are evident for both the 2° $\times$ 2.5° and 4° $\times$ 5° SASS simulations, with the increase being greater below 288 K for the 4° $\times$ 5° SASS, and between 288 and 310 K for the 2° $\times$ 2.5° SASS simulation. The general increase of relative angular momentum for the surface-to-310-K layer, however, is larger for the 2° $\times$ 2.5° than the 4° $\times$ 5° simulations, indicating that the vortex for the 2° $\times$ 2.5° SASS simulation is better organized and extends through a deeper isentropic layer. This increase stems from the greater intensity of the 2° $\times$ 2.5° mass circulation and the resulting net inward transport of angular momentum. The relative angular momentum in layers above 310 K has decreased compared to that at the initial time period. This decrease aloft is a reflection of the development of a warm-core gradient-balanced circulation that, at least in the relative sense, is simply better organized and deeper in the 2° $\times$ 2.5° simulations than in the 4° $\times$ 5° simulations.

Vertical profiles at 12-h increments for the 7.5° budget volume of mass-weighted area-averaged relative angular momentum (Fig. 15) show the time evolution

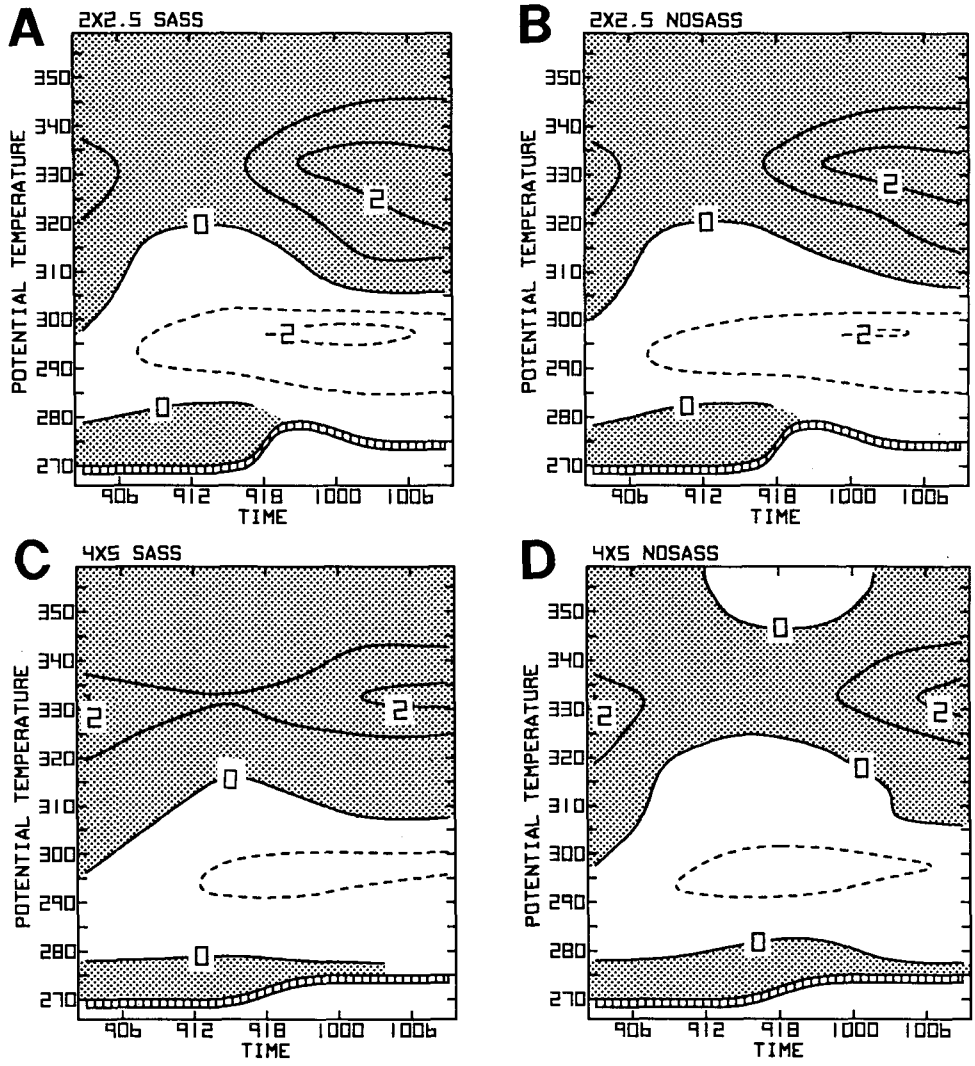

FIG. 12. Isentropic time sections of eddy mode of lateral absolute angular momentum transport (10^{17} kg m^2 s^{-2}) as in Fig. 6.

of the spinup of the vortex for the 2° × 2.5° SASS simulation. From 0000 to 1200 UTC 9 September, the low- to midlevel relative angular momentum increases somewhat. From 1200 UTC 9 to 0000 UTC 10 September, the vertical redistribution of relative angular momentum is striking as the relative angular momentum in the lower layer doubles, while the angular momentum in the upper layers decreases significantly. This period coincides with the strengthening of the isentropic mass circulation during the onset of rapid cyclogenesis in combination with a net downward transfer of angular momentum by the total torque. Note in Fig. 9 that for the total torque the region of strong positive torque occurs in the layer of greatest increase within the 280–290-K layer, while negative torque persists throughout the overlaying isentropic layers for most of this period. In the last 12 h, the relative angular momentum increases in the middle isentropic layers as the vortex grows in intensity and vertical extent. This rapid buildup of the relative angular momentum is associated with the period of rapid deepening of the cyclone and largest values of heating.

e. Water vapor budget

In order to help isolate possible reasons for the increased heating in the 2° × 2.5° SASS simulation compared to the NOSASS simulation, the water vapor budget was evaluated. The time sections of lateral water vapor transport (Fig. 16) show larger inward transport in the lower isentropic layers for the 2° × 2.5° SASS compared to the 2° × 2.5° NOSASS simulation

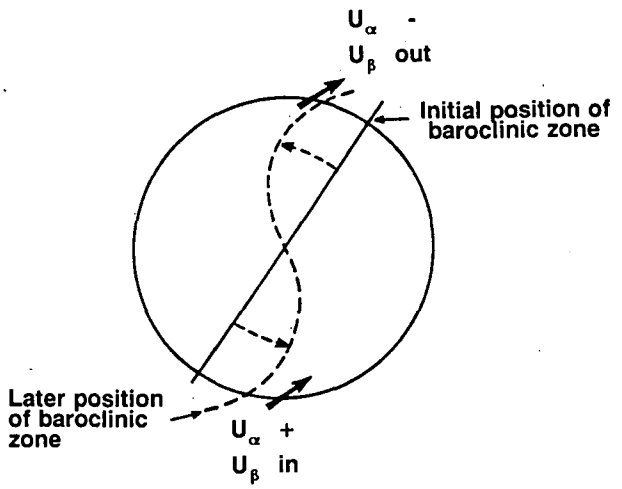

FIG. 13. Schematic illustrating the covariance of storm-relative radial and tangential velocities associated with rotation and deformation of the thermal field (after Johnson and Hill 1987).

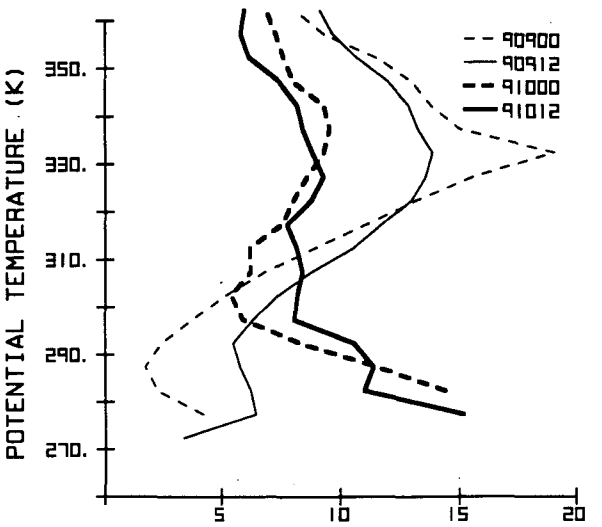

FIG. 15. Vertical profiles of mass-weighted area-averaged relative angular momentum (10^7 m^2 s^{-1}) for 7.5° budget volume for 2° × 2.5° SASS simulation from 0000 UTC 9 September to 1200 UTC 10 September 1978 in 12-h increments.

throughout most of the 36-h simulation. For the early period of rapid cyclogenesis, from 1200 UTC 9 through 0000 UTC 10 September, the inward water vapor transport for 2° × 2.5° SASS is more than 25% larger than for either the 2° × 2.5° NOSASS or 4° × 5° simulations. The larger lateral transport is associated with an increased time tendency of water vapor (Fig. 17) in the 290–315-K layer from 1200 UTC through 1800 UTC 9 September for the 2° × 2.5° SASS simulation compared to the other three simulations. The lateral water vapor transport for the 4° × 5° SASS and NOSASS simulations becomes larger from 1800 UTC 9 to 1200 UTC 10 September reaching values similar to those of the 2° × 2.5° SASS simulation. During this period, the deepening rate of the surface cyclone increases for the 4° × 5° SASS simulation, but the deepening rate remains much less than the maximum deepening rates for the 2° × 2.5° simulations. The increased deepening rate of the 2° × 2.5° SASS simulation over the 4° × 5° simulation is a reflection of the overall improvement in this simulation of the angular momentum exchange and upward diabatic mass transport at small radii that is so important for the accurate simulation of vortices in gradient balance.

The major changes in the lateral water vapor transport between the SASS and NOSASS simulations occurred in the lower isentropic layers. Therefore, to isolate one of the possible reasons for the differences in

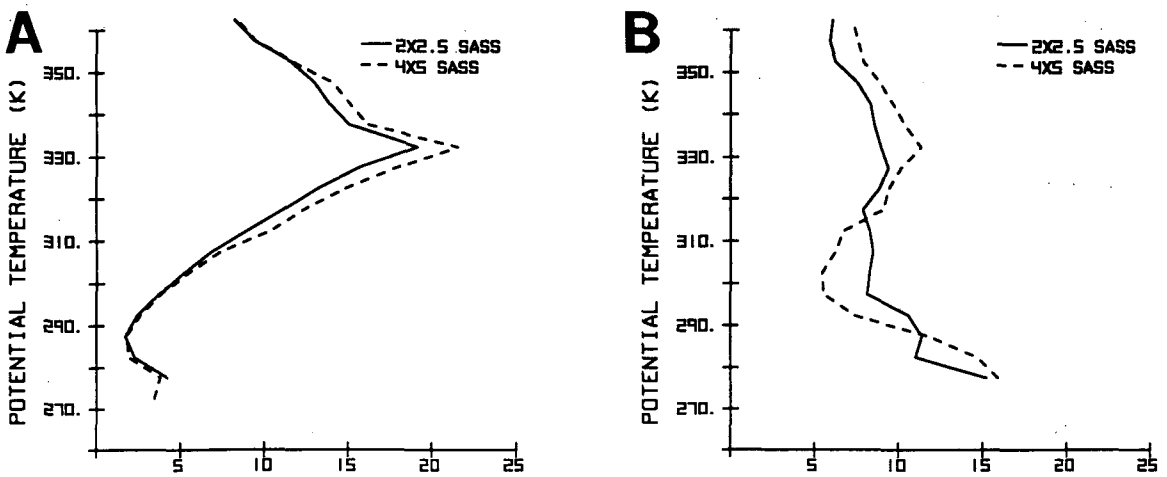

FIG. 14. Vertical profiles of mass-weighted area-averaged relative angular momentum (10^7 m^2 s^{-1}) for 7.5° budget volume for 2° × 2.5° SASS and 4° × 5° SASS simulations at (a) 0000 UTC 9 September 1978 and (b) 1200 UTC 10 September 1978.

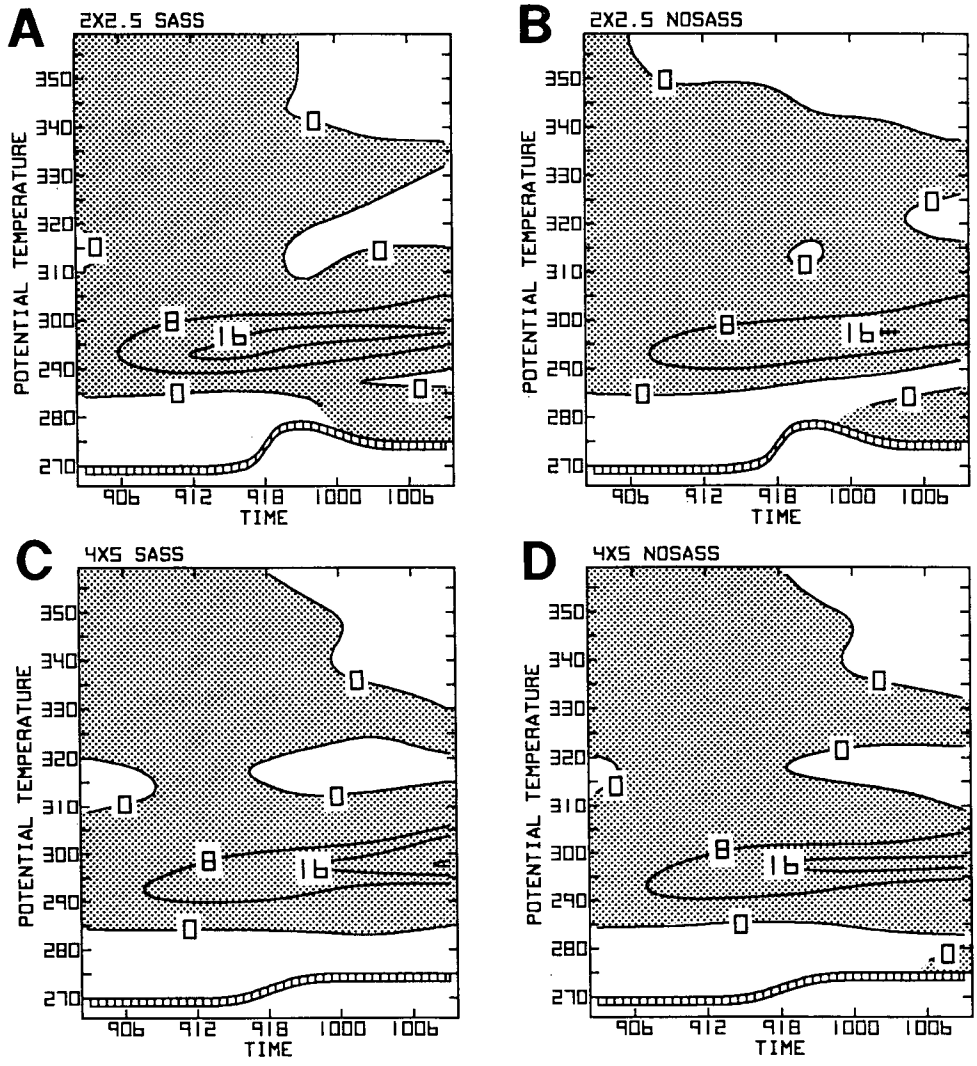

FIG. 16. Isentropic time sections of lateral water vapor transport (10^7 g s^{-1}) as in Fig. 6.

water vapor transport, the specific humidity of the 2° × 2.5° SASS and NOSASS simulations for the lowest sigma layer is shown for 0000 UTC 9 September in Fig. 18. The specific humidity in the drier air to the north of the east–west-oriented frontal zone is similar between the SASS and NOSASS initial conditions. However, the specific humidity in the moister tropical air to the south of the front and the developing *QE II* cyclone is 1–2 g kg^{-1} higher in the SASS compared to the NOSASS initial conditions (Fig. 4c). The moisture difference farther south in the central Atlantic Ocean is up to 4 g kg^{-1}. Physical processes that likely account for the increased water vapor are changes in surface fluxes of water vapor and changes in horizontal transports of water vapor due to the inclusion of SASS winds during the prior 48-h assimilation. At the initial time period, 0000 UTC 9 September, the low-level airflow was more southerly just off the east coast of the United States (noted in section 4a, Fig. 4), which would have also contributed initially to increasing the advection of water vapor into the region where the explosive deepening of the *QE II* cyclone would occur. The higher specific humidities of the air in the warm sector of the cyclone likely contributed to the increased inward lateral transport of water vapor and the increased latent heat release observed in the 2° × 2.5° SASS simulation.

The qualitative characteristics of the water vapor balance are also evident in distributions of the Eulerian water vapor convergence in the lowest sigma layer for 0000 UTC 10 September and the 6-h accumulated precipitation from 0000 UTC to 0600 UTC 10 September (Figs. 19 and 20). These distributions show that the water vapor convergence and accumulated

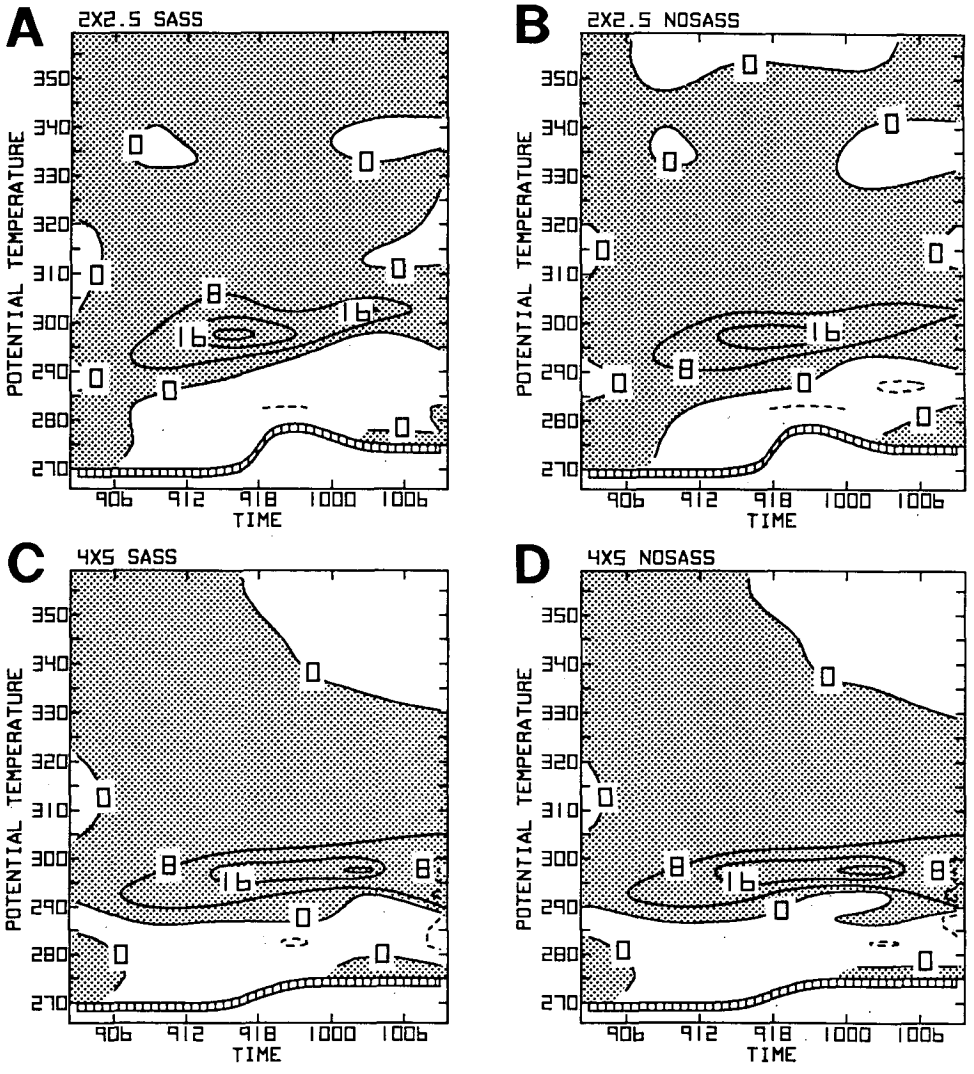

FIG. 17. Isentropic time section of time tendency of water vapor (10^7 g s^{-1}) as in Fig. 6. Regions of positive tendency are stippled.

precipitation for the 2° × 2.5° simulations are a factor of 3 or more larger than those for the corresponding 4° × 5° simulations. The moisture convergence and 6-h accumulated precipitation for the 2° × 2.5° SASS simulation are 50% greater than that for the 2° × 2.5° NOSASS simulation. In contrast, the moisture convergence for the 4° × 5° SASS simulation is only marginally greater than that for the 4° × 5° NOSASS simulation, while the 6-h accumulated precipitation is similar for both 4° × 5° simulations.

These results are in qualitative agreement with the quasi-Lagrangian analysis in that the hydrological cycle of the cyclone diagnosed in the 2° × 2.5° simulations is much stronger than in the 4° × 5° simulations. Also, the impact of adding the SASS winds on the respective components of the hydrologic cycle is much larger in the case of the 2° × 2.5° simulations than in the 4° × 5° simulations.

f. Kinetic energy budget

The complete kinetic energy budget of the *QE II* storm was evaluated. For the sake of brevity, however, only the terms that showed the most significant changes between the SASS and NOSASS simulations will be shown and discussed.

The vertical time section of the lateral kinetic energy transport (Fig. 21) for the 2° × 2.5° SASS simulation shows inward transport in upper isentropic layers throughout the storm's development, but the vertical extent and magnitude of the inward transport decrease with time. After 1800 UTC 9 September, outward lat-

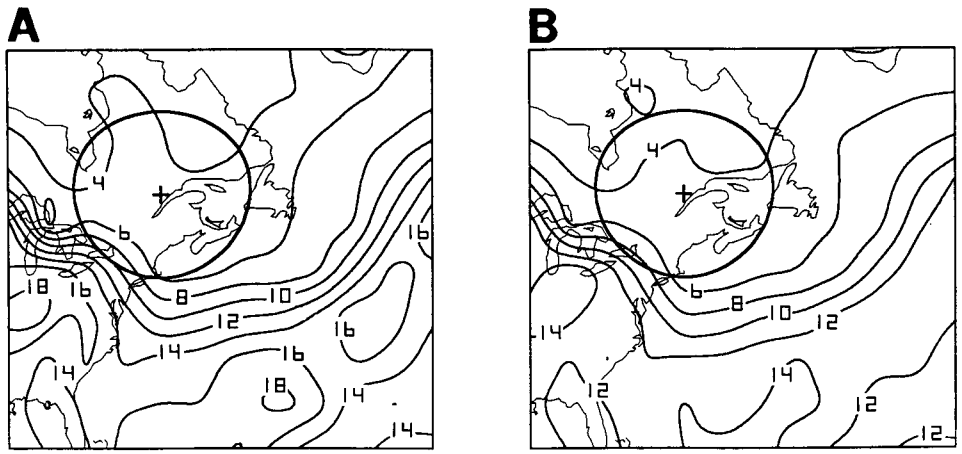

FIG. 18. Specific humidity (g kg^{-1}) in the lowest sigma layer at 0000 UTC 9 September 1978 for (a) 2° × 2.5° SASS and (b) 2° × 2.5° NOSASS simulations. Areal location of 7.5° budget volume indicated by circle.

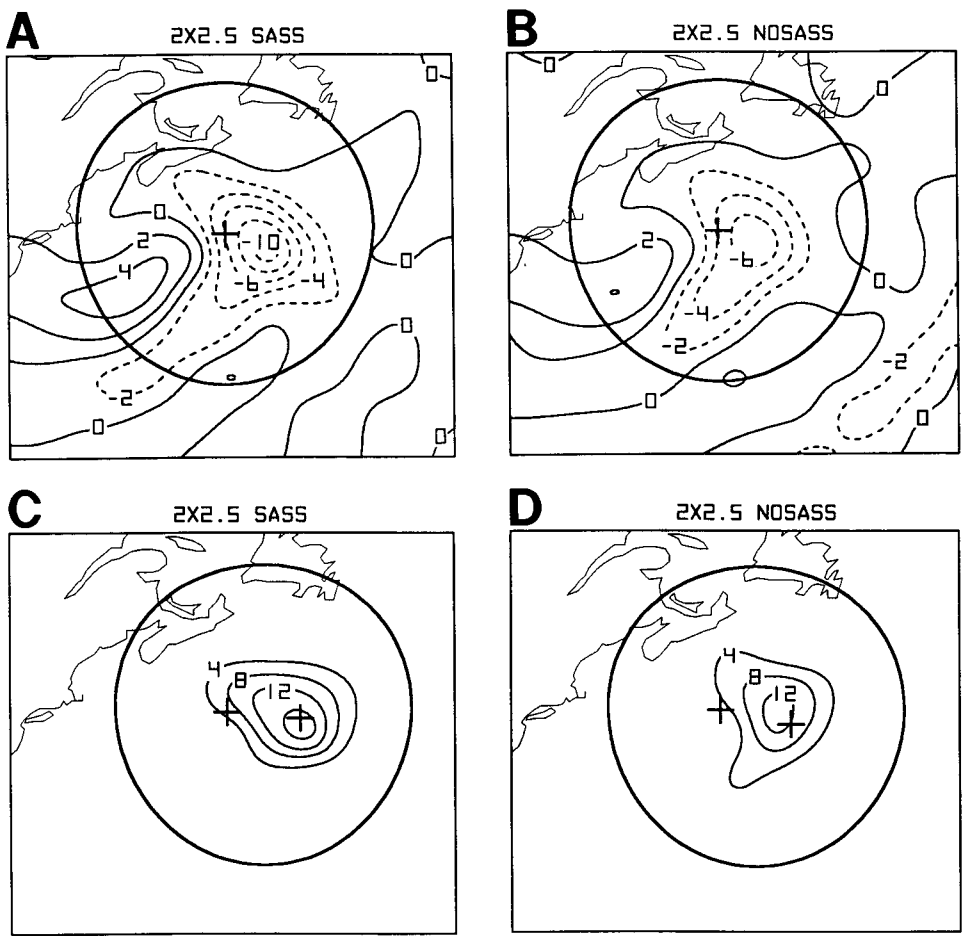

FIG. 19. Eulerian water vapor convergence (10^{-4} g s^{-1}) in the lowest model sigma layer for 0000 UTC 10 September 1978 for (a) 2° × 2.5° SASS and (b) 2° × 2.5° NOSASS, and 6-h accumulated precipitation (cm day^{-1}) from 0000 UTC to 0600 UTC 10 September 1978 for (c) 2° × 2.5° SASS and (d) 2° × 2.5° NOSASS. Location of 7.5° budget volume shown by circle. In (c) and (d) the circle is centered at the location of the position at 0300 UTC, while the "+" symbols are positions at 0000 UTC (left) and 0600 UTC (right).

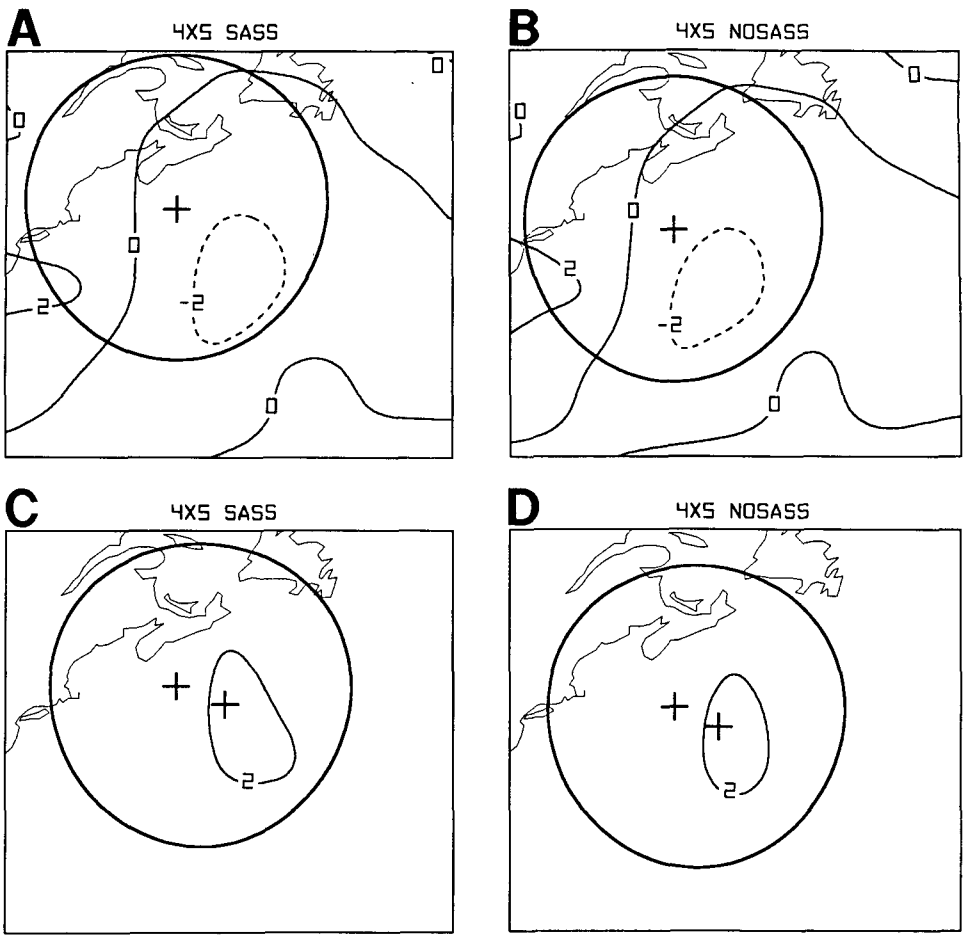

FIG. 20. Eulerian water vapor convergence in the lowest model sigma layer for 0000 UTC 10 September 1978 for (a) 4° × 5° SASS and (b) 4° × 5° NOSASS, and 6-h accumulated precipitation from 0000 UTC to 0600 UTC 10 September 1978 for (c) 4 × 5 SASS and (d) 4 × 5 NOSASS as in Fig. 19.

eral transport develops in the 305–325-K layer, increasing in magnitude as the storm develops. The weak outflow below 290 K is primarily due to the movement of the cyclone away from colder air in the lowest isentropic layers. The pattern of outward and inward lateral kinetic energy transport is qualitatively similar for the NOSASS simulation. However, after 0000 UTC 10 September, the outward lateral transport in the 305–325-K layer is substantially larger for 2° × 2.5° SASS than for 2° × 2.5° NOSASS.

The lateral transport of kinetic energy for the 4° × 5° SASS and NOSASS simulations are much different than for the 2° × 2.5° simulations. Strong inward kinetic energy transport occurs in upper isentropic layers throughout the development. The magnitude of the inward transport decreases with time. A small layer of outward kinetic energy transport develops in the 310–320-K layer at the very end of the development, but is much less than in either 2° × 2.5° simulation. The 4° × 5° simulations lack the signature of any significant outward transport of kinetic energy from the storm.

The vertical time section of the area-averaged kinetic energy generation (Fig. 22) for the 2° × 2.5° SASS simulation shows a sink of kinetic energy in the 300–360-K layer from 0000 to 2100 UTC 9 September. After 2100 UTC 9 September, the magnitude and vertical extent of the sink region decreases as a region of positive kinetic energy generation develops in the 280–330-K layer. The lower layer of positive generation is associated with frictionally induced cross-isobar flow in the planetary boundary layer as the storm develops and translates rapidly. The upper positive generation regions are probably associated with cross-isobar flow in the jet-stream region.

The general distributions of the positive and negative regions of the kinetic energy generation are similar in the NOSASS simulation. The major difference occurs between 1800 UTC 9 September and 1200 UTC 10 September, when the upper-level negative region is more negative and the positive region is smaller in extent and significantly weaker in magnitude. This is also true in the lower-level positive region, and especially

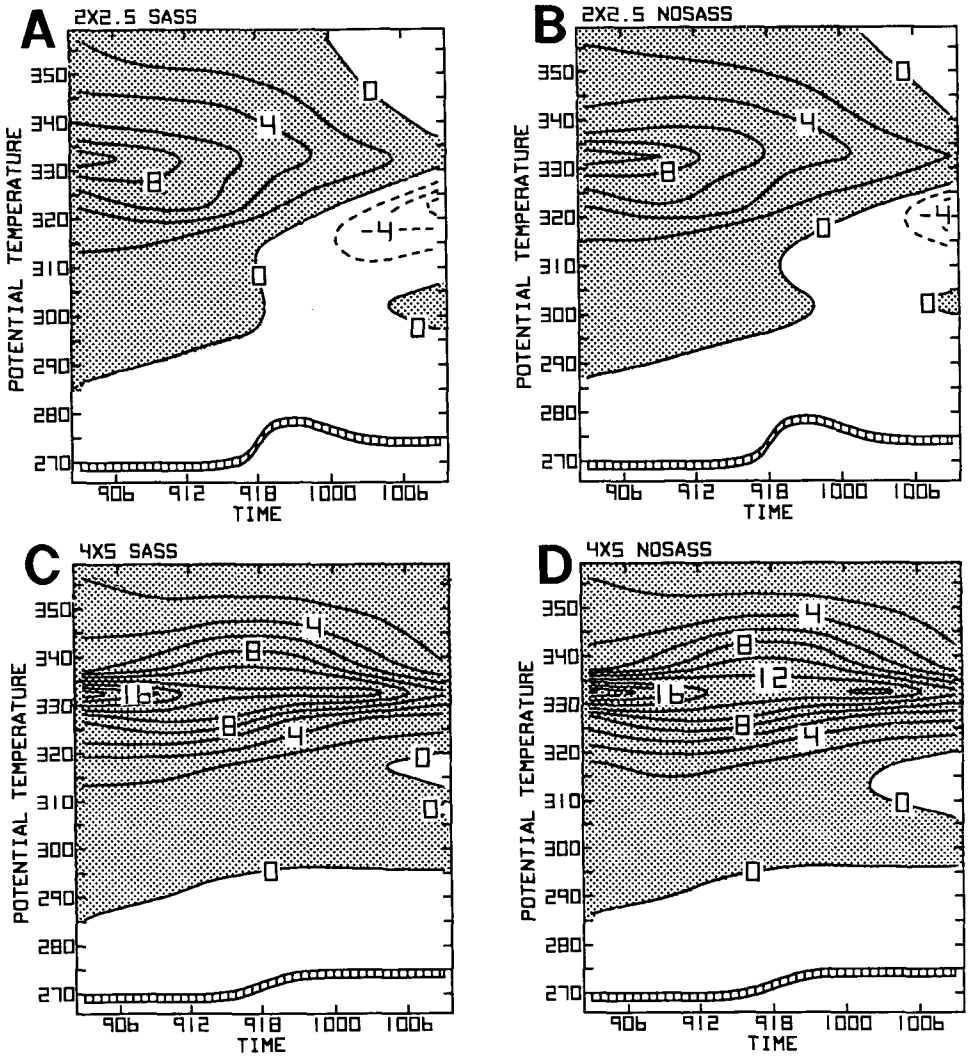

FIG. 21. Isentropic time sections of lateral kinetic energy transport (W m^{-2}) as in Fig. 6. Lateral transport is divided by the area of the budget volume. This is equivalent to the area-averaged divergence of kinetic energy transport.

true of the region from 315 to 330 K. Thus, for the NOSASS simulation, the positive generation of kinetic energy is less both in the planetary boundary layer and in upper jet-stream levels.

The 4° × 5° SASS and NOSASS simulations show a sink of kinetic energy above 300 K throughout the development. A slight area of positive generation develops in the layer below 300 K. The kinetic energy generation in the 4° × 5° simulations is much less than in either 2° × 2.5° simulation.

Comparing the temporal and vertical distributions of the lateral mass transport and kinetic energy generation, a general pattern in upper layers is evident, with layers of inward kinetic energy transport also being layers of negative generation and layers of outward kinetic energy transport also being layers of positive generation. This general pattern was also evident in the kinetic energy budget studies of the moist development stages of the Midwest cyclone of 26–28 May 1973 and the Alberta cyclone of 30 March–2 April 1971 (Spaete 1988).

Substantial temporal changes of kinetic energy throughout the storm development are evident in the vertical profiles of mass-weighted area-averaged kinetic energy shown for 0000 UTC 9 September (Fig. 23a) and 1200 UTC 10 September (Fig. 23b). At the initial time period, small values of kinetic energy occur in the lower isentropic layers due to the weak circulation in surface layers, while a peak of kinetic energy occurs at the 330–335-K layer in the upper-level jet-stream level. Notable differences occur in the 330–335-K layer for the 4° × 5° simulation compared to the 2° × 2.5° simulation. These initial differences are attributed to truncation errors introduced by additional vertical in-

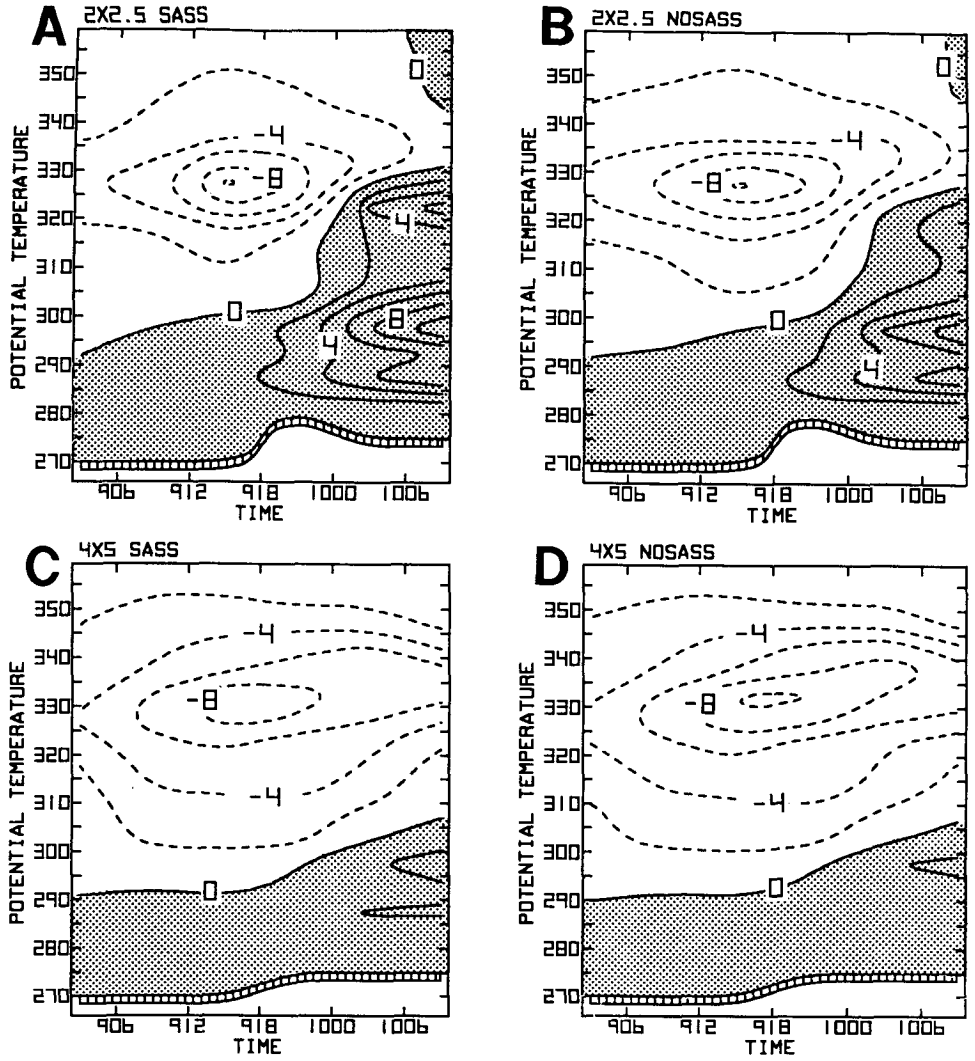

FIG. 22. Isentropic time sections of area-averaged kinetic energy generation (W m^{-2}) as in Fig. 6. Regions of positive generation are stippled.

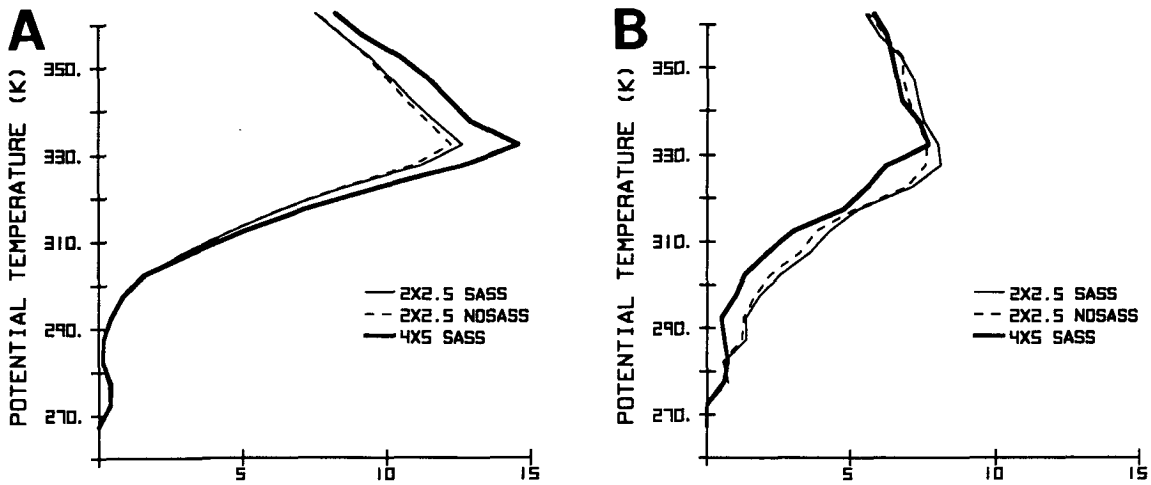

FIG. 23. Vertical profiles of mass-weighted area-averaged kinetic energy (10^2 m^2 s^{-2}) for 7.5° budget volume for 2° × 2.5° SASS, 2° × 2.5° NOSASS, and 4° × 5° SASS simulations at (a) 0000 UTC 9 September 1978 and (b) 1200 UTC 10 September 1978.

terpolations performed in the specification of the 2° × 2.5° initial conditions from the 4° × 5° assimilation results.

By 1200 UTC 10 September, the area-averaged kinetic energy has increased significantly throughout most of the 280–315-K layer for both 2° × 2.5° simulations. The kinetic energy above the 315-K layer has decreased significantly for all the simulations between 0000 UTC 9 and 1200 UTC 10 September. At 1200 UTC 10 September, the kinetic energy for the 2° × 2.5° simulations is larger than for the 4° × 5° SASS simulation in the 280–330-K layer.

5. Summary

This case study of the *QE II* storm focused on the effect of inclusion of SASS data and horizontal grid resolution on the model simulation. Quasi-Lagrangian diagnostics of mass and absolute angular momentum budgets were compared and contrasted for simulations with SASS and NOSASS winds in the initial conditions and for resolutions of 2° × 2.5° and 4° × 5°. The 2° × 2.5° simulations provided more accurate predictions of the *QE II* cyclone, with a more intense low-level circulation and an improved storm track than the 4° × 5° simulations. The 2° × 2.5° SASS simulation was the best, with a storm track closest to that observed and with the deepest cyclone.

The improvements from the 2° × 2.5° simulations were associated with more intense lateral mass transports than in the 4° × 5° simulations. Maximum heating rates were doubled in the 2° × 2.5° compared to the 4° × 5° simulations. The inclusion of SASS data also increased the intensity of the mean lateral mass transport, and significantly increased the maximum heating rate.

In agreement with Eliassen's perspective on the forcing of the horizontal mass circulation by torques, the distribution of the total torque is in good agreement (with reversed sign) with the distribution of the lateral mass transport. The distribution of the total torque is more organized in the 2° × 2.5° simulations than in the 4° × 5° simulations.

The distributions of the pressure and inertial torques, and eddy mode of lateral absolute angular momentum transport are also more temporally and vertically organized for the 2° × 2.5° simulations. The upper-level positive eddy mode is larger for the 2° × 2.5° simulations. This is linked in part to the increased horizontal resolution of the baroclinic structure and the rotation of the low-level baroclinic zone. Vertical profiles of mass-weighted area-averaged relative angular momentum show that the low-level spinup was more intense, and through a deeper layer for the 2° × 2.5° simulations.

During the early explosive deepening of the cyclone, the inward lateral transport of water vapor in lower layers was larger for the 2° × 2.5° SASS simulation than in the 2° × 2.5° NOSASS simulation. For the lowest sigma layer of the model at the initial time period, 0000 UTC 9 September, the specific humidity in the tropical air to the south of the developing cyclone was 1–2 g kg^{-1} moister in the SASS simulation than in the NOSASS simulation. This moister tropical air in conjunction with the more southerly low-level winds off the east coast of the United States in the SASS initial conditions likely contributed to the increased inward lateral transport of water vapor and to the increased latent heat release in the 2° × 2.5° SASS simulation compared to the 2° × 2.5° NOSASS simulation.

The lateral kinetic energy transport was inward in upper isentropic layers for all the simulations in the early part of the storm development. The 2° × 2.5° simulations developed an outward lateral kinetic energy transport in the 305–325-K layer after 1800 UTC 9 September. The outward lateral kinetic energy transport was larger in the 2° × 2.5° SASS simulation than in the NOSASS simulation. The kinetic energy generation was negative in upper isentropic layers for all four simulations in the early storm development. The generation for the 2° × 2.5° simulations became positive after 2100 UTC 9 September and was larger for the SASS than NOSASS simulations. The low-level kinetic energy increases were much larger for the 2° × 2.5° simulations compared to the 4° × 5° simulations with the 2° × 2.5° SASS simulations having the largest kinetic energy increase.

This case study of the *QE II* for simulations comparing SASS versus NOSASS data and high versus low resolution is an example of the ability of the quasi-Lagrangian analysis to isolate consistent physical processes that jointly are related to subtle differences in predictive skill of models resulting from the impact of satellite data. The major improvement in predictive skill for the *QE II* storm stemmed from the increase in horizontal resolution. However, when comparing the predictive skill of SASS versus NOSASS initial fields, the comparison of quasi-Lagrangian transport processes clearly reveals a better defined and more intense isentropic mass circulation and vertical diabatic mass flux from SASS simulations even though differences in the mean sea level surface pressure pattern between SASS and NOSASS simulations were quite subtle. Underlying reasons for a similar positive impact of satellite data in the prediction of cyclogenesis in the lee of the Rockies were identified by Vergin et al. (1984) using quasi-Lagrangian diagnostics.

Acknowledgments. The authors express appreciation to Todd Schaack and Dr. Russ Schneider for helpful comments. We also wish to acknowledge the helpful comments made by two anonymous reviewers. We gratefully acknowledge the assistance of Judy Mohr for assistance in typing the manuscript, and Cindy Karls, Christine Johnson, and Michelle Novak in drafting the figures. This work was supported in part by NASA

Grant NAG 5-81 and in part by the NASA Scatterometer (NSCAT) Project.

APPENDIX A

Isentropic Quasi-Lagrangian Storm Budget

Define:

$$F = \int_{V_\theta} \rho J_\theta f r^2 \sin\beta dV_\theta,$$

where f is any specific property per unit mass.

Budget equation:

$$\frac{dF}{dt} = S(F) + \mathrm{LT}(F) + \mathrm{VT}(F),$$

where

lateral transport is

$$\mathrm{LT}(F) = -\int_{\theta_B}^{\theta_T}\int_0^{2\pi} \rho J_\theta (U - W)_\beta f r \sin\beta d\alpha d\theta|_{\beta_B},$$

vertical transport is

$$\mathrm{VT}(F) = \int_0^{\beta_B}\int_0^{2\pi} \rho J_\theta \dot{\theta} f r^2 \sin\beta d\alpha d\beta|_{\theta_B},$$

source is

$$S(F) = \int_{V_\theta} \rho J_\theta \frac{df}{dt} r^2 \sin\beta dV_\theta.$$

Boundary conditions:

$$\rho J_\theta \dot{\theta}_T = 0$$

$$\rho J_\theta \dot{\theta} = 0; \quad \theta < \theta_s(\alpha, \beta, t)$$

$$\theta_s = \theta(\alpha, \beta, r_s, t) = \text{earth's surface.}$$

Storm angular momentum:

$$\mathbf{g}_a = (\mathbf{r} - \mathbf{r}_0) \times (\mathbf{U}_a - \mathbf{W}_{o_a}).$$

Component of $\mathbf{g}_a$ along $\mathbf{r}_0$, the storm axis of rotation:

$$g_{a_z} = \mathbf{k}_o \cdot \mathbf{g}_a = r \sin\beta (U_a - W_{o_a})_\alpha.$$

Time rate of change of g_{a_z}:

$$\dot{g}_{a_z} = r \sin\beta \left(\frac{1}{r \sin\beta} \frac{\partial \psi}{\partial \alpha_\theta} + F_\alpha + \dot{W}_{o_{a_\alpha}} + \mathbf{W}_{o_a} \cdot \frac{\mathbf{g}_a}{r} \right),$$

where the four sources of angular momentum are the pressure, frictional, and inertial torques, and a translational source, respectively.

Kinetic energy:

$$k = \frac{\mathbf{U} \cdot \mathbf{U}}{2}.$$

Time rate of change of kinetic energy:

$$\frac{dk}{dt} = -\mathbf{U} \cdot \nabla_\theta \psi_M,$$

where $\psi_M = c_p T + gz$.

Decomposition of lateral mass transport into mean and eddy modes:

$$\mathrm{VT}(F) = \mathrm{MM}(F) + \mathrm{EM}(F),$$

where the mean mode is

$$\mathrm{MM}(F) = -\int_{\theta_B}^{\theta_T}\int_0^{2\pi} \overline{\rho J_\theta} \widehat{(U - W)}_\beta^\alpha (\hat{f}^\alpha) r \sin\beta d\alpha d\theta|_{\beta_B};$$

eddy mode is

$$\mathrm{EM}(F) = -\int_{\theta_B}^{\theta_T}\int_0^{2\pi} \overline{\rho J_\theta} \widehat{(U - W)_\beta^* f^*}^\alpha r \sin\beta d\alpha d\theta|_{\beta_B}.$$

APPENDIX B

List of Symbols

F	budget volume integral of arbitrary property
J_θ	Jacobian of transformation from height to potential temperature, $\lvert\partial z/\partial\theta\rvert$
V_θ	volume with limits of integration defined by (α, β, θ)
R	gas constant
c_p	specific heat at constant pressure
g	acceleration due to gravity
g_{a_z}	component of absolute angular momentum along storm's axis of rotation
α	azimuthal coordinate
β	radial coordinate
ρ	density
θ	potential temperature
$\mathbf{U}$	earth-relative wind velocity
$\mathbf{W}$	earth-relative velocity of lateral boundary
$\mathbf{g}_a$	absolute angular momentum
$\mathbf{r}$	position vector

Subscripts and superscripts

B	bottom or boundary
T	top of atmosphere
a	absolute frame of reference
o	denotes budget volume central reference axis
s	surface of earth
α	azimuthal component
β	radial component
θ	isentropic coordinate system; isentropic surface

Operators

$\cdot$	Substantial derivative
$\overline{\ }$	Azimuthal average, $(2\pi)^{-1}\int_0^{2\pi}(\ )d\alpha$
$\hat{\ }^\alpha$	Mass-weighted azimuthal average $\overline{\rho J_\theta(\ )}/\overline{\rho J_\theta}$
$*$	Deviation from mass-weighted azimuthal average

REFERENCES

Anderson, D., A. Hollingsworth, S. Uppala, and P. Woiceshyn, 1991: A study of the use of scatterometer data in the European Centre for Medium-Range Weather Forecasts operational analysis-forecast model. 2: Data impact. *J. Geophys. Res.*, **96,** 2635–2647.

Anthes, R. A., Y-H. Kuo, and J. R. Gyakum, 1983: Numerical simulations of a case of explosive marine cyclogenesis. *Mon. Wea. Rev.*, **111,** 1174–1188.

Atlas, R., 1987: The role of oceanic fluxes and initial data in the numerical prediction of an intense coastal cyclone. *Dyn. Atmos. Oceans,* **10,** 359–388.

——, E. Kalnay, and M. Halem, 1985: The impact of satellite temperature sounding and wind data on numerical weather prediction. *Opt. Eng.*, **24,** 341–346.

——, A. J. Busalacchi, M. Ghil, S. Bloom, and E. Kalnay, 1987: Global surface wind and flux fields from model assimilation of Seasat data. *J. Geophys. Res.*, **92,** 6477–6487.

Baker, W. E., R. Atlas, E. Kalnay, M. Halem, P. M. Woiceshyn, S. Peteherych, and D. Edelmann, 1984: Large-scale analysis and forecast experiments with wind data from the Seasat-A scatterometer. *J. Geophys. Res.*, **89,** 4927–4936.

——, S. C. Bloom, J. S. Woollen, M. S. Nestler, E. Brin, T. W. Schlatter, and G. W. Branstator, 1987: Experiments with a three-dimensional statistical objective analysis scheme using FGGE data. *Mon. Wea. Rev.*, **115,** 272–296.

Duffy, D. G., and R. Atlas, 1986: The impact of Seasat-A scatterometer data on the numerical prediction of the *Queen Elizabeth II* storm. *J. Geophys. Res.*, **91,** 2241–2248.

——, ——, T. Rosmond, E. Barker, and R. Rosenberg, 1984: The impact of Seasat scatterometer winds on the Navy's operational model. *J. Geophys. Res.*, **89,** 7238–7244.

Eliassen, A., 1951: Slow thermally or frictionally controlled meridional circulation in a circular vortex. *Astrophys. Norv.*, **5,** 19–60.

Gallimore, R. G., and D. R. Johnson, 1981: A numerical diagnostic model of the zonally averaged circulation in isentropic coordinates. *J. Atmos. Sci.*, **38,** 1870–1890.

Gyakum, J. R., 1983: On the evolution of the *QE II* storm. I: Synoptic aspects. *Mon. Wea. Rev.*, **111,** 1137–1155.

——, 1991: Meteorological precursors to the explosive intensification of the *QE II* storm. *Mon. Wea. Rev.*, **119,** 1105–1131.

Hale, R., 1983: Mass and angular momentum diagnostics of the intense Ohio Valley extratropical cyclone of 25–27 January 1978. M.S. thesis, University of Wisconsin—Madison, 96 pp.

Halem, M., E. Kalnay-Rivas, W. E. Baker, and R. Atlas, 1982: An assessment of the FGGE satellite observing system during SOP-1. *Bull. Amer. Meteor. Soc.*, **63,** 407–426.

Helfand, H. M., J. Pfaendtner, and R. Atlas, 1987: The effect of increased horizontal resolution on GLA fourth order model forecasts. *Short and medium-range numerical weather prediction—Collection of papers presented at the WMO/IUGG NWP symposium,* Tokyo, WMO/IUGG NWP, 303–315.

Ingleby, N. B., and R. A. Bromley, 1991: A diagnostic study of the impact of SEASAT scatterometer winds on numerical weather prediction. *Mon. Wea. Rev.*, **119,** 84–103.

Johnson, D. R., 1974: The absolute angular momentum of cyclones. *Subsynoptic Extratropical Weather Systems: Observations, Analysis, Modeling, and Prediction,* Volume II seminars and workshops, Colloquium notes of the advanced study program and small-scale analysis and prediction project, National Center for Atmospheric Research, Boulder, CO, 821 pp. [NTIS PB-247286.]

——, and W. K. Downey, 1975a: Azimuthally averaged transport and budget equations for storms: Quasi-Lagrangian diagnostics 1. *Mon. Wea. Rev.*, **103,** 967–979.

——, and ——, 1975b: The absolute angular momentum of storms: Quasi-Lagrangian diagnostics 2. *Mon. Wea. Rev.*, **103,** 1063–1076.

——, and ——, 1976: The absolute angular momentum budget of an extratropical cyclone: Quasi-Lagrangian diagnostics 3. *Mon. Wea. Rev.*, **104,** 3–14.

——, and D. K. Hill, 1987: Quasi-Lagrangian diagnostics of a Mediterranean cyclone: Isentropic results. *Meteor. Atmos. Phys.*, **36,** 118–140.

——, C. H. Wash, and R. A. Petersen, 1976: The mass and absolute angular momentum budgets of the Alberta cyclone of 30 March–2 April 1971. Preprints, *Sixth Conf. Weather Forecasting and Analysis,* Albany, Amer. Meteor. Soc., 350–356.

Kalnay, E., R. Balgovind, W. Chao, D. Edelmann, J. Pfaendtner, L. Takacs, and K. Takano, 1983: Documentation of the GLAS fourth order general circulation model. Vol. 1 Model documentation. NASA Tech. Memo. 86064, 371 pp. [Available from NASA Goddard Space Flight Center, Greenbelt, MD.] [NTIS N8424048.]

Kalnay-Rivas, E., A. Bayliss, and J. Storch, 1977: The 4th order GISS model of the global atmosphere. *Beitr. Phys. Atmos.*, **50,** 299–311.

Katzfey, J. J., 1978: A diagnostic study of the vertical redistribution of angular momentum in isentropic coordinates by pressure torques. M.S. thesis, University of Wisconsin—Madison, 118 pp.

Kuo, Y.-H., M. A. Shapiro, and E. G. Donall, 1991: The interaction between baroclinic and diabatic processes in a numerical simulation of a rapidly intensifying extratropical marine cyclone. *Mon. Wea. Rev.*, **119,** 368–384.

Palmén, E., and C. W. Newton, 1969: *Atmospheric Circulation Systems.* Academic Press, 603 pp.

Spaete, P. E., 1988: Kinetic energy diagnostic studies of extratropical cyclones based on storm relative motion. Ph.D. thesis, University of Wisconsin—Madison, 270 pp.

Stoffelen, A. C. M., and G. J. Cats, 1991: The impact of *Seasat-A* scatterometer data on high-resolution analysis and forecasts: The development of the *QE II* storm. *Mon. Wea. Rev.*, **119,** 2794–2802.

Uccellini, L. W., 1986: The possible influence of upstream upper level baroclinic processes on the development of *QE II* storm. *Mon. Wea. Rev.*, **114,** 1019–1027.

Vergin, J. M., D. R. Johnson, and R. Atlas, 1984: A quasi-Lagrangian diagnostic case study of the effect of satellite sounding data assimilation on model cyclone prediction. *Mon. Wea. Rev.*, **112,** 725–739.

Wash, C. W., 1978: Diagnostics of observed and numerically simulated extratropical cyclones. Ph.D. thesis, University of Wisconsin—Madison, 215 pp.

Yu, T.-W., and R. D. McPherson, 1984: Global data assimilation experiments with scatterometer winds from Seasat-A. *Mon. Wea. Rev.*, **112,** 368–376.